Bioactive Materials 28 (2023) 167–182

Contents lists available at ScienceDirect

Bioactive Materials

journal homepage: www.keaipublishing.com/en/journals/bioactive-materials

Vanillin-based functionalization strategy to construct multifunctional microspheres for treating inflammation and regenerating intervertebral disc

Zhuang Zhu [a,1], Qifan Yu [a,1], Hanwen Li [a], Feng Han [a], Qianping Guo [a], Heng Sun [a], He Zhao [c], Zhengdong Tu [a], Zhuang Liu [b,***], Caihong Zhu [a,**], Bin Li [a,*]

[a] Orthopedic Institute, Department of Orthopedic Surgery, The First Affiliated Hospital, School of Biology & Basic Medical Sciences, Suzhou Medical College, Soochow University, Suzhou, Jiangsu, 215007, China
[b] Institute of Functional Nano & Soft Materials, Jiangsu Key Laboratory for Carbon-Based Functional Materials and Devices, Soochow University, Suzhou, Jiangsu, 215123, China
[c] Children's Hospital of Soochow University, Pediatric Research Institute of Soochow University, Suzhou, Jiangsu, 215123, China

ARTICLE INFO

Keywords:
Intervertebral disc degeneration
Microsphere
Vanillin
Transforming growth factor β3
Regeneration

ABSTRACT

Intervertebral disc degeneration (IVDD) is one of the main causes of low back pain. Although local delivery strategies using biomaterial carriers have shown potential for IVDD treatment, it remains challenging for intervention against multiple adverse contributors by a single delivery platform. In the present work, we propose a new functionalization strategy using vanillin, a natural molecule with anti-inflammatory and antioxidant properties, to develop multifunctional gelatin methacrylate (GelMA) microspheres for local delivery of transforming growth factor β3 (TGFβ3) toward IVDD treatment. *In vitro*, functionalized microspheres not only improved the release kinetics of TGFβ3 but also effectively inhibited inflammatory responses and promoted the secretion of extracellular matrix (ECM) in lipopolysaccharide-induced nucleus pulposus (NP) cells. *In vivo*, functionalized platform plays roles in alleviating inflammation and oxidative stress, preserving the water content of NP and disc height, and maintaining intact structure and biomechanical functions, thereby promoting the regeneration of IVD. High-throughput sequencing suggests that inhibition of the phosphatidylinositol 3-kinase (PI3K)-Akt signaling might be associated with their therapeutic effects. In summary, the vanillin-based functionalization strategy provides a novel and simple way for packaging multiple functions into a single delivery platform and holds promise for tissue regeneration beyond the IVD.

1. Introduction

Low back pain (LBP) is an extremely common musculoskeletal symptom that affects about 60%–80% of people during their lifetimes [1]. Disability-adjusted life-years (DALYs) impacted by LBP increased by 46.9% from 1990 to 2019, making it the leading cause of disability worldwide [2]. What's more, LBP places a heavy burden on social health care and economic development globally [3,4]. Intervertebral disc degeneration (IVDD) is a widely accepted cause of LBP and is thought to be strongly associated with pain severity [1]. Although the pathophysiology of IVDD has not been fully defined, numerous studies have confirmed that several adverse contributors are clearly associated with degeneration: a disordered microenvironment with overactive inflammation and oxidative stress, the imbalance of anabolism/catabolism in the extracellular matrix (ECM) [5,6].

The intervertebral disc (IVD) is the largest avascular tissue in the body. ECM breakdown products generated during dysfunction or damage may be responsible for the initiation of local inflammation by promoting the secretion of pro-inflammatory cytokines from nucleus pulposus cells (NPCs), such as interleukin-1β (IL-1β), interleukin-6 (IL-

Peer review under responsibility of KeAi Communications Co., Ltd.
* Corresponding author. Rm 201 Bldg Jiwu, Soochow University (North Campus), 178 Ganjiang Rd, Suzhou, Jiangsu, 215007, China.
** Corresponding author.
*** Corresponding author.
E-mail addresses: zliu@suda.edu.cn (Z. Liu), zhucaihong@suda.edu.cn (C. Zhu), binli@suda.edu.cn (B. Li).
[1] These authors contributed equally to this work.

https://doi.org/10.1016/j.bioactmat.2023.05.005
Received 14 February 2023; Received in revised form 25 April 2023; Accepted 9 May 2023

6), and tumor necrosis factor-α (TNF-α) [7]. The interactions of these cytokines with receptors promote the production of chemokines and the infiltration of blood vessels and immune cells, leading to further amplification of the inflammatory cascade. A further imbalance between supply and demand within the inflammatory IVD microenvironment is caused by excess reactive oxide species (ROS) from mitochondrial dysfunction, upregulated matrix metalloproteinases (MMPs) expression, and the loss of cellular phenotypes and physiological functions [5,8]. These drastic changes in homeostasis lead to the extensive remodeling and degeneration of the IVD. The current clinical treatments for IVDD include conservative and surgical therapies according to the severity of the patient's symptoms. However, these therapies can only relieve symptoms caused by herniation, cannot reverse degeneration, and patients are still at risk of recurrence [9]. Injections of drugs or growth factors into discs have also been reported in some studies to inhibit localized inflammation or provide biological clues for repair. However, given their short half-life and rapid clearance *in vivo*, reaching a significant level of efficacy usually requires iterative intradiscal injections, thereby increasing the risk of IVDD and dose-dependent side effects [10]. The use of a biomaterial-based delivery platform is an ideal strategy for the treatment of IVDD as it permits the targeted delivery of therapeutic factors and a high degree of bioavailability.

Various delivery platforms have been employed to facilitate the treatment of IVDD. Of these, microspheres have significant clinical potential and are being developed on a large scale [11,12]. Microspheres have good biocompatibility, degradability, mechanical properties, and injectability in addition to favorable drug encapsulation rates and delivery efficiency, making them show exciting potential for use in humans, especially in the treatment of cancer, diabetes, and osteoarthritis [13–15]. Such desirable properties also allow for targeted delivery and controlled drug release, making them suitable for localized diseases, including IVDD. For example, poly (ester amide) (PEA) microspheres have been designed and employed in the loading and local delivery of celecoxib [16] or acetonide [17] into the IVD. In addition to anti-inflammatory drugs, more kinds of therapeutic factors have been employed for local delivery with microspheres. Cell-based therapies for treating IVDD, particularly mesenchymal stem cells (MSCs) or NPCs supplementation, have been evaluated for the past two decades and have been found to be effective [18]. However, the clinical utilization of such cell-based therapies may be limited by immunogenicity, tumorigenicity, and difficulties with regulatory approval [19]. Autologous cell recruitment and enhancement using growth factors may be promising for innovative cell-free therapy. Transforming growth factor β3 (TGFβ3) is a potent anabolic growth factor that promotes cell proliferation, differentiation, migration, and ECM production and has been widely used for cartilage and tendon repair [20,21]. Recent works have shown that TGFβ3 plays an important role in promoting the viability and ECM production of NPCs [22–24]. Microspheres have been also developed to allow for loading and local delivery of TGFβ3 to support the growth and chondrogenic differentiation of MSCs and NPCs [25]. On the one hand, it is the most important feature of biomaterial carriers to improve the release kinetics of growth factors, determining their therapeutic outcomes and clinical applications [26]. On the other hand, single-factor administration, either to inhibit inflammation or promote ECM synthesis, is still insufficient for treating the complex pathogenesis of IVDD [27,28]. Therefore, this study aims to construct a kind of multifunctional microsphere that can both improve the release kinetics of TGFβ3 and regulate the harsh microenvironment to overcome the limitations of single-factor management for IVDD therapy.

Vanillin (4-hydroxy-methoxybenzaldehyde) is a naturally occurring aromatic aldehyde that contains a hydroxyl group and is widely found in many plants [29]. Vanillin with anti-inflammatory, antioxidant, and antibacterial properties, can scavenge ROS and inhibit the signaling pathways associated with inflammation, permitting its use in the treatment of inflammatory diseases [30,31]. Compared with commonly used anti-inflammatory drugs, vanillin possesses more active groups in its simple structure. In other words, it can be more easily designed to participate in the polymerization and further chemical modification of biomaterials. Kang et al. designed the poly (vanillin oxalate) as a novel polymeric nanoparticle via acetal linkages and peroxalate ester bons that can release vanillin to cure liver damages by inhibiting inflammation and apoptosis [32]. The reactive aldehyde groups contained in vanillin polymers were also found to be responsible for the formation of Schiff base bonds with amino-modified poly-tetrahydropyridine, resulting in the quick formation of a dynamic hydrogel to cure subcutaneous infections [33]. Vanillin was also found to reduce the number of senescent cells and maintain the phenotype of IVD cells by inhibiting inflammation and increasing extracellular vesicle release and/or uptake [34]. Its advantageous pharmacology and structure made vanillin to be one of the ideal candidates for this study.

In the present work, a vanillin-based strategy was proposed to develop multifunctional gelatin methacrylate (GelMA) microspheres via microfluidic technology. After modification, vanillin can be easily decorated onto GelMA microspheres in one step by the copolymerization of vanillin methacrylate (VMA) and GelMA. On the one hand, vanillin might still retain its anti-inflammatory and antioxidant properties after modification. On the other hand, vanillin on the microspheres would serve as a "bridge" to load and control the long-term release of TGFβ3, due to the dynamic covalent bonds formed between their aldehyde groups and numerous amino groups on the protein (Scheme 1). Then, *in vitro* experiments verified the performances of vanillin-grafted microspheres as functionalized carriers in TGFβ3 release, NPCs recruitment, adhesion, and proliferation, as well as their efficacies in inhibiting inflammation and regulating the anabolism/catabolism in lipopolysaccharide (LPS) induced NPCs. In addition, RNA sequencing (RNA-seq) was used to reveal the underlying molecular mechanism, suggesting that the therapeutic effects may be associated with its inhibition of the phosphoinositide 3-kinase (PI3K)-Akt signaling pathway. Finally, experiments in the rat IVDD model tested the effects of the functionalized system in eliminating excess ROS, maintaining the disc height, water content, intact structure, and biomechanical function of tissue, enhancing ECM deposition and regeneration of the IVD.

2. Materials and methods

2.1. Microsphere fabrication

Microspheres were prepared using a coaxial needle with the inner and outer sizes of 30 G and 28 G, respectively. The outer needle and the microfluidic device were connected by a syringe loaded with mineral oil (ST1524, Beyotime, China) and 5% (w/w) Span 80 (S110839, Aladdin, China), which represented the continuous phase. A hydrogel prepolymer solution that consisted of 7 wt% GelMA with 60% substitution (EFL-GM-60, EFL, China) and 0.05 wt% lithium phenyl (2,4,6-trimethylbenzoyl) phosphinate (LAP) was served as the dispersed phase. VMA (Changyan chemical technology Co. LTD, Shanghai, China) was also introduced into the prepolymer to a concentration of 1 mg/mL when preparing GelMA microspheres grafted by VMA (V@GM). The jetting flow mode and ideal size were obtained by adjusting the flow rate of the two phases, and the uniform droplets downstream of the needle synchronously polymerized on the crosslinking disk under ultraviolet (UV) irradiation (with a wavelength of 405 nm) to obtain fresh GelMA microspheres (GM) and V@GM. The collected microspheres were washed repeatedly with isopropanol and 75% ethanol to remove continuous phase. They were then washed thoroughly with phosphate buffered saline (PBS). The cleaned microspheres were frozen at −80 °C and then freeze-dried for 48 h.

2.2. Microsphere characterization

The morphologies of the fresh and dried microspheres were observed using a bright-field microscope (Zeiss Axiobert 200, USA) and a scanning electron microscope (SEM, FEI, USA). The diameter distribution of

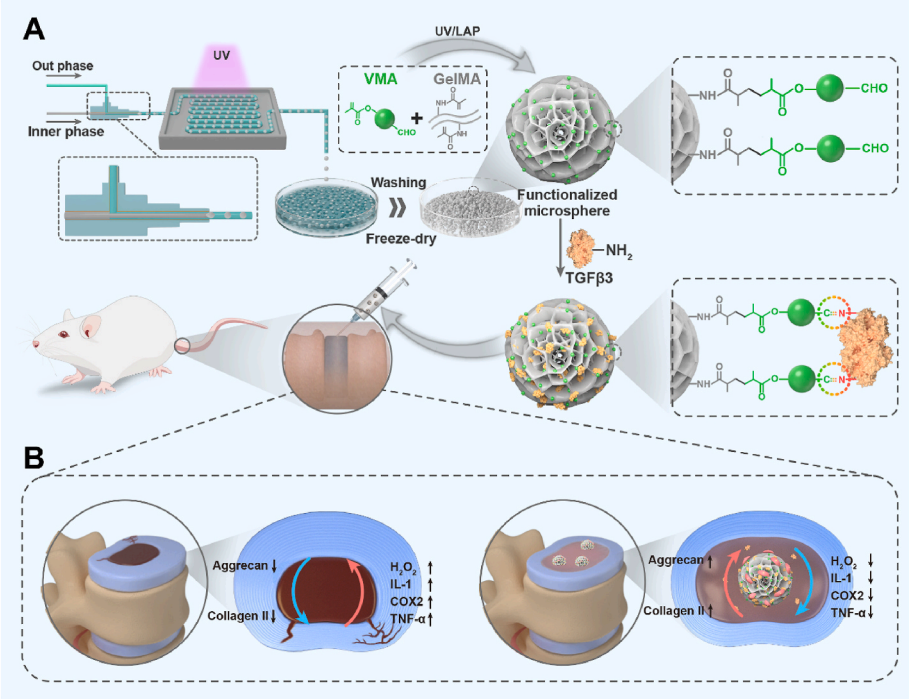

Scheme 1. Summary of fabricating vanillin functionalized microspheres for the IVD regeneration. (A) The detailed method and process of fabricating vanillin functionalized microspheres. (B) The mechanism for the IVD regeneration.

the microspheres was analyzed by mearing 50 microspheres using Image J software (NIH, Bethesda, USA). GM and V@GM were characterized and analyzed using a fourier-transform infrared spectroscope (FTIR, Nicolet iS 10, Thermo Fisher Scientific, USA). Briefly, the flakes were prepared with a potassium bromide grinding tablet and scanned 128 times in the range of 400–4000 cm^{-1} at a resolution of 4 cm^{-1}. The rheological properties of the microspheres were tested with a Discovery HR2 Hybrid Rheometer (TA Instrument, USA). GM and V@GM were spread on Peltier plates. Frequency sweeps (0.1–10 Hz frequency and 1% strain at 37 °C) were then performed to obtain a storage modulus (G′) and loss modulus (G″).

2.3. Measurements of TGFβ3 loading and release

The two kinds of microspheres (GM and V@GM) were prepared and then three groups of parallel samples were set up. Freeze-dried microspheres (1 mg) were immersed in 1 mL of PBS solution that contained 100 ng/mL TGFβ3 at 37 °C for 12 h. The concentrations of TGFβ3 in the remaining solutions were measured to calculate the microsphere payload. Microspheres were put into 2 mL of PBS with 1% bovine serum albumin (BSA), and then placed in a thermostatic shaker at 37 °C at 80 cycles min^{-1}. At specific time points (2 h, 4 h, 8 h, 12 h, 1 d, 3 d, 5 d, 7 d, 10 d, and 14 d), 1 mL of supernatant was taken and supplemented with the same amount of PBS. The TGFβ3 concentration in the diluted supernatant (1:100) was tested with a TGFβ3 enzyme-linked immunosorbent assay (ELISA, Elabscience, China), and the release curves were drawn.

2.4. Cell viability and proliferation on the microspheres

To evaluate the effects of VMA on cell proliferation, NPCs were cultured on microspheres grafted with different concentrations of VMA (0, 0.5, 1, and 2 mg/mL) for 1, 3, and 7 days. And five groups of parallel samples were set up. The cell-laden microspheres were incubated in a medium containing 10% cell counting kit-8 (CCK-8) solution (Dojin Laboratories, Kumamoto, Japan) for 2 h at different time points. A microplate reader (BioTek Instruments, USA) was used to measure the absorbance at 450 nm. To evaluate the viability of NPCs in different groups, a live/dead cell viability assay was performed using a live/dead stain kit (Inbitrogen, USA). After 3-day cultures in different microspheres (GM and V@GM), cell-laden microspheres were stained at room temperature for 30 min by the live/dead working solutions. And there are three parallel samples of both groups. The cells on the microspheres were observed under a fluorescence microscope (Carl Zeiss Microscopy, Thornwood, NY, USA).

2.5. Transwell assay

To rule out the effect of cell proliferation, the NPCs and different microspheres were resuspended in DMEM/F12 medium supplemented with 2% FBS. A total of 2×10^4 NPCs with 100 μL medium were placed in the upper chamber of a 24-well transwell plate (Corning, NY, USA). GM, V@GM, T@GM, and V-T@GM were placed on the lower chambers of the plate on 500 μL of medium, allowing for the creation of three groups of parallel samples. We used 8 h as a time point. The membrane was then washed with PBS and incubated in 4% paraformaldehyde at room temperature. After the NPCs on the upper chamber were wiped off with a cotton swab, cells were stained with 0.1% crystal violet solution (Beyotime, Nanjing, China) for observation and quantitation. Cells that migrated into the bottom chamber were counted manually in 3 random fields under 40 × magnifications.

2.6. RT-qPCR analysis

NPCs cultured on different microspheres, then five groups were assigned in this part: (i) NPCs cultured on GM in cultured medium without LPS (GM group), (ii) NPCs cultured on GM in cultured medium with 1 μg/mL LPS (GM' group), (iii) NPCs cultured on T@GM in cultured medium with 1 μg/mL LPS (T@GM group), (iv) NPCs cultured on V@GM in cultured medium with 1 μg/mL LPS (V@GM group), (v) NPCs cultured on V-T@GM in cultured medium with 1 μg/mL LPS (V-T@GM group). There are three parallel samples of each group. RNA from the

NPCs was extracted using TRIzol reagent (Invitrogen, Carlsbad, CA, USA) after 3 days' culture. RNA concentrations were then measured using NanoDrop 2000 spectrophotometers (Thermo Fisher Scientific, Waltham, MA, USA). RNA was converted into first-strand cDNA for a quantitative polymerase chain reaction. The primer sequences (Sangon Biotech, Shanghai, China) of the genes used in our study are listed in Table S1. The relative mRNA expression of each gene was normalized to the housekeeping gene *Gapdh* and analyzed using the $2^{-\Delta\Delta Ct}$ method.

2.7. Immunofluorescence

NPCs were cultured on different microspheres, then five groups were assigned in this part like those described above. There are three parallel samples of each group. They were fixed in 4% paraformaldehyde and then permeabilized with 0.3% Triton X-100 in PBS for 10 min after a 5-days culture. The microspheres were then soaked in Immunol Staining Blocking Buffer (Beyotime, Shanghai, China) for 1 h to block nonspecific binding. After incubation with 1:100 diluted *anti*-COX2 or 1:200 diluted anti-Col II antibodies at 4 °C overnight, Alexa Fluor® 488 antibodies (1:1000, Abcam Cambridge, UK) were used for fluorescent labeling. The nuclei were stained with DAPI and observed by the inverted fluorescence microscope. The primary antibodies are listed in Table S2.

2.8. RNA-seq and bioinformatic analyses

NPCs were cultured on GM and V-T@GM treated with LPS for 3 days, and 3 groups of parallel samples were set. The RNA was extracted from the NPCs with TRIzol reagent (Invitrogen, Carlsbad, CA, USA). RNA libraries were sequenced on the illumine Novaseq™ 6000 platform by LC Bio Technology CO, Ltd (Hangzhou, China). To be specific, after total RNA was extracted, dynabeads oligo (dT) beads (Thermo fisher, USA) were used for specific capture of mRNA from total RNA. Then the mRNA was fragmented into short fragments using divalent cations under elevated temperature (Magnesium RNA Fragmentation Module under 94 °C 5–7min). Then the cleaved RNA fragment was reverse-transcribed to create the cDNA by SuperScriptTM Reverse Transcriptase (Invitrogen, USA), which were next used to synthesize U-labeled second-stranded DNAs with *E. coli* DNA polymerase I (NEB, USA), RNase H (NEB, USA) and dUTP Solution (Thermo Fisher, USA). An A-base was then added to the blunt ends of each strand, preparing them for ligation to the indexed adapters. Each adapter contained a T-base overhang for ligating the adapter to the A-tailed fragmented DNA. Dual-index adapters were ligated to the fragments, and size selection was performed with AMPureXP beads. After the heat-labile UDG enzyme (NEB, USA) treatment of the U-labeled second-stranded DNAs, the ligated products were amplified with PCR by the following conditions: initial denaturation at 95 °C for 3 min; 8 cycles of denaturation at 98 °C for 15 s, annealing at 60 °C for 15 s, and extension at 72 °C for 30 s; and then final extension at 72 °C for 5 min. The average insert size for the final cDNA libraries was 300 ± 50 bp. At last, we performed the 2 × 150bp paired-end sequencing (PE150) on an Illumina NovaseqTM 6000 (LC-Bio Technology CO., Ltd., China) following the vendor's recommended protocol. Genes differential expression analysis was performed by DESeq2 software between two different groups (and by edgeR between two samples). The genes with the parameter of false discovery rate (FDR) below 0.05 and absolute fold change ≥2 were considered differentially expressed genes. GO terms meeting conditions with $p < 0.05$ were defined as significantly enriched GO terms in DEGs. Pathways meeting conditions with $p < 0.05$ were defined as significantly enriched pathways in DEGs. We performed gene set enrichment analysis using software GSEA (v4.1.0) and MSigDB to identify whether a set of genes in specific GO terms and KEGG pathways show significant differences in the two groups. Briefly, we input the gene expression matrix and rank genes by Signal2Noise normalization method. Enrichment scores and p value was calculated in default parameters. GO terms, KEGG pathways meeting this condition with |NES|>1, NOM p-val<0.05, and FDR q-val<0.25 were considered to be different in the two groups. All sequencing reads were entered into the China National GeneBank DataBase (CNGBdb).

2.9. Animal model and surgical procedures

All procedures followed the NIH Guide for the Care and Use of Laboratory Animals and were approved by the Institutional Animal Care and Use Committee of Soochow University (SUDA20220711A04). A total of 80 adult male rats aged 10–12 weeks and weighing about 350 g were purchased from the Experimental Animal Center of Soochow University and randomly divided into five groups. The rat caudal vertebral degeneration model was established using a previously described experimental method [35]. Rats were anesthetized via intraperitoneal injection of pentobarbital, and routine disinfection and towel spreading were performed on the puncture points. To avoid the influence from between adjacent degenerative segments, a 20G needle was used to percutaneously pass through the segments of caudal vertebrae 7–8 (Co7-8) and 9–10 (Co9-10) into the middle of the NP tissue (the depth controlled at 5 mm) and confirmed with X-ray (Fig. S10). The needle was rotated 360° after passing through the annulus and maintained for 30 s to ensure a degeneration effect. Five groups were assigned in this study: (i) no needle puncture (sham group), (ii) the needle puncture and PBS injection (defect group), (iii) the needle puncture and injection of GelMA microspheres loaded with TGFβ3 (T@GM group), (iv) the needle puncture and injection of vanillin conjugated microspheres (V@GM group), (v) the needle puncture and injection of vanillin conjugated microspheres loaded with TGFβ3 (V-T@GM group). All injections of microspheres were performed immediately after acupuncture with a micropump, and the disc injection volume was 10 μL. The rats were transferred to a warm and ventilated environment after the operation. All rats were fed in a clean and ventilated environment with 25 °C and 50% humidity.

2.10. Fabrication of Lipo@HRP&ABTS nanoprobes and the detection of H_2O_2 at the NP sites

Lipo@HRP&ABTS nanoprobes were prepared according to methods established in a previous study [36]. Briefly, the 1,2-dihexadecanoyl-*sn*-glycero-3-phosphocholine, cholesterol, 2,2′-azinobis-(3-ethylbenzthiazoline-6-sulphonate (ABTS), and 1,2-distearoyl-*sn*-glycero-3-phosphoethanolamine-*N*-(amino-(polyethyleneglycol)-2000) (DSPE-PEG), were dissolved in methanol at the molar ratio of 6:4:12:0.5. The solution was condensed to form a lipid film with rotary evaporation, after which 1 mL of PBS solution containing horseradish peroxidase (HRP) was added. The compound was sonicated at 65 °C followed by rehydration with five freeze-thaw cycles. The suspension was then extruded 50 times through a 200-nm mesh filter at 50 °C. A S-300 Sephadex column was used to purify the Lipo@HRP&ABTS nanoprobes. On the 7th day after surgery, 10 μL of Lipo@HRP&ABTS nanoprobes were locally injected into the NP tissue site. After 15 min, a layer of ultrasonic gel was coated onto the skin overlying the injured IVDs, and the detector of the Vevo LAZR Imaging System (FUJIFILM VisualSonics Inc.) was placed onto the skin covering the injured IVD. The level of H_2O_2 was then measured.

2.11. Radiology evaluation

X-ray and MRI imaging operations were performed on the caudal vertebrae of rats after surgery for 4 and 8 weeks. All rats were anesthetized and placed in a supine position with their tails straight. The disc height index (DHI) as measured on X-ray images was calculated with ImageJ software for between-group comparisons (DHI = twice the sum of the anterior, middle, and posterior edge heights of the intervertebral space/the sum of the anterior, middle, and posterior heights of the adjacent vertebral bodies, DHI% = measured DHI/sham group DHI at

each time point × 100%) (Fig. S11) [35]. The T2-weighted images of the caudal spine were obtained with a 1.5T MRI scanner (Magnetom Essenza, Siemens Medical Solution, Erlangen, Germany), and the NP signal was measured using ImageJ software.

2.12. Histological analysis

Specimens were respectively harvested on the 4th and 8th week and fixed in 10% formaldehyde solution for 24 h. After decalcification with 14% ethylene diamine tetraacetic acid (EDTA) for 30 days, samples were embedded in paraffin and sliced to a thickness of 6 μm. Further, hematoxylin and eosin (H&E) staining was performed to examine tissue histology. The changes and distribution of collagen and proteoglycans were evaluated using safranin O-fast green (SO/FG) staining. The histological grading system was divided into 4 categories as previously described by Masuda (Table S3), ranging from 4 (normal) to 12 points (severe degeneration) [37]. To evaluate the *in vivo* changes to COL II, ACAN, and COX2, sections were stained via immunohistochemical staining after antigen retrieval. Briefly, all sections were performed heat mediated antigen retrieval with sodium citrate buffer pH 6.5 for 15 min at 85 °C. Then they were put into a 3% H_2O_2 solution and incubated at room temperature without light for 15 min. After being washed with PBS 3 times, they were blocked with Immunol Staining Blocking Buffer (Beyotime, Shanghai, China) for 1 h. The slices were incubated with primary antibodies (1:200 diluted anti-COL II antibodies, 1:200 diluted *anti*-ACAN antibodies, or 1:200 diluted *anti*-COX2 antibodies) overnight at 4 °C followed by an HRP-labeled secondary antibody (1:100 diluted) at room temperature for 1 h. Samples were stained with 3,3′-diaminobenzidine (DAB) for 30 s, and the nuclei were counterstained with hematoxylin. Images were taken and viewed with light microscopy. The primary antibodies used are listed in Table S2.

2.13. Biomechanical tests

The IVDs were stored in PBS at 4 °C after the surrounding tissue was exfoliated. When testing its compressive properties, the sample underwent a single loading cycle. Uniaxial compression tests were performed at a speed of 0.2 mm/min until the displacement reached 10% of the height of the IVD. The height and the diameters of the IVDs were measured with a vernier caliper. Stress was calculated as the force/the area of the IVD, and the strain was calculated as displacement/the height of the IVD. Three specimens were tested in each group. Compression modulus was calculated from the stress-strain curves according to a previously published method. And the stress relaxation properties of the IVDs were measured according to a previous study [38]. In brief, the IVDs were compressed to a 10% strain with a deformation rate of 1 mm/min. The strain was held constant for 300 s, while the force was recorded as a function of time.

2.14. Statistical analysis

All quantitative data were presented as the mean ± standard deviation (SD) of at least three independent repetitions in each group. Statistical analysis was performed using one-way ANOVA methods, followed by Tukey's multiple comparisons test (GraphPad Prism 8 software, CA, USA). The difference was considered statistically significant if the p value was less than 0.05.

3. Results

3.1. Preparation and characterization of microspheres

Based on the co-flow shearing between oil and water, droplets were formed downstream of a coaxial needle in the microfluidic device. GelMA microspheres (GM) and functionalized microspheres modified with VMA (V@GM) were obtained via further cross-linking and freeze-drying. The microspheres could be resized by adjusting the flow of the oil and water, and the diameter of the microspheres negatively correlated with oil flow (Fig. S1A). Under the field of the light microscope, it was observed that fresh GMs with different diameters prepared with microfluidics were characterized by an intact shape, uniform size, and good dispersion (Fig. 1A). Diameters were approximately 320 μm and 150 μm when the oil and water flow rates were 20/1 and 40/1, respectively (Fig. 1B). Previous studies have reported that smaller microgels (diameter <300 μm) could enhance mass transport to/from cells to achieve a more efficient nutrient and waste exchange due to a larger surface-to-volume ratio [39], plus to ensure the smoother injection, the microspheres with diameters of 150 μm were used for subsequent experiments. The results of the degradation experiment results showed that microspheres degraded only about 30% after 14 days in PBS solution at 37 °C and could be maintained for about 6 days in the PBS with 2 U/mL collagenase type I solution (Figs. S1B and C). The surface structure, chemical bonds, and mechanical properties of the microspheres were analyzed to verify the successful linkage of vanillin into the microsphere. V@GM retained its porous structure compared with GM, as shown in the SEM images (Fig. 1C). FTIR spectra showed that, compared with the GM group, the increased absorption strength at 1689 cm^{-1} in the V@GM group may be due to the increased C═C structure that resulted from the introduction of the VMA. Its *C*–O structure contributed to the changes in the relative intensity of the *C*–O stretching vibration peak at 1087 cm^{-1} and 1027 cm^{-1}. Together with the obvious blue shift of the absorption peak near 3534 cm^{-1}, which may be attributed to the breaking of hydrogen bonds in the hydrogel microsphere caused by small molecules, these measurements indicated that VMA grafting was successful (Fig. 1D). The rheological properties of the microspheres around the 1% strain and 0.1–10 Hz frequency showed a similar storage modulus (G′) but different loss modulus (G″) between groups (Fig. 1E), which may be due to the dynamic covalent bonds formed between the aldehyde groups of VMA and the amino groups of GelMA.

3.2. Biocompatibility of functionalized microspheres in vitro

The biocompatibility of GM and V@GM was demonstrated with CCK-8 test and live/dead cell staining. The results of CCK-8 test on the 1st, 3rd, and 7th day showed that there is no significant difference between the control group and the V@GM group when the concentration of VMA did not exceed 1 mg/mL ($p > 0.05$). However, cell proliferation was inhibited when the VMA concentration reached 2 mg/mL ($p < 0.05$) (Fig. S2). Then, the dose-dependent anti-inflammatory effect of the molecule was demonstrated by quantification of gene expression levels of *Il1b* and *Il6* in LPS-induced NPCs cultured on microspheres containing 0.5 mg/mL or 1 mg/mL VMA (Fig. S3). Therefore, the one with the higher concentration of VMA was used in the following experiments. Further, live/dead cell staining on the 3rd day showed that the survival rate of the NPCs cultured in both the GM and V@GM groups was high, and the number of dead cells was almost negligible (Fig. S4A). Cytoskeletal staining images showed that NPCs cultured on both microspheres exhibited good adhesion and spreading on the 3rd day (Fig. S4B). These results suggested that functionalized microspheres prepared by VMA at 1 mg/mL had satisfying biocompatibility to provide physiological and spatial supports for the adhesion and proliferation of NPCs on them.

3.3. The potential of functionalized microspheres as a delivery platform

To further explore the potential of functionalized microspheres as delivery platforms, we tested the loading and release of TGFβ3 from microspheres using an ELISA kit. The standard concentration curve is shown in Fig. S5A. Loading of TGFβ3 was 14.7 ± 0.9 ng/mg in the GM group and 18.7 ± 1.2 ng/mg in the V@GM group (Fig. S5B). After loading TGFβ3, the GelMA microspheres grafted with or without vanillin were defined as V-T@GM or T@GM, respectively. A burst release could

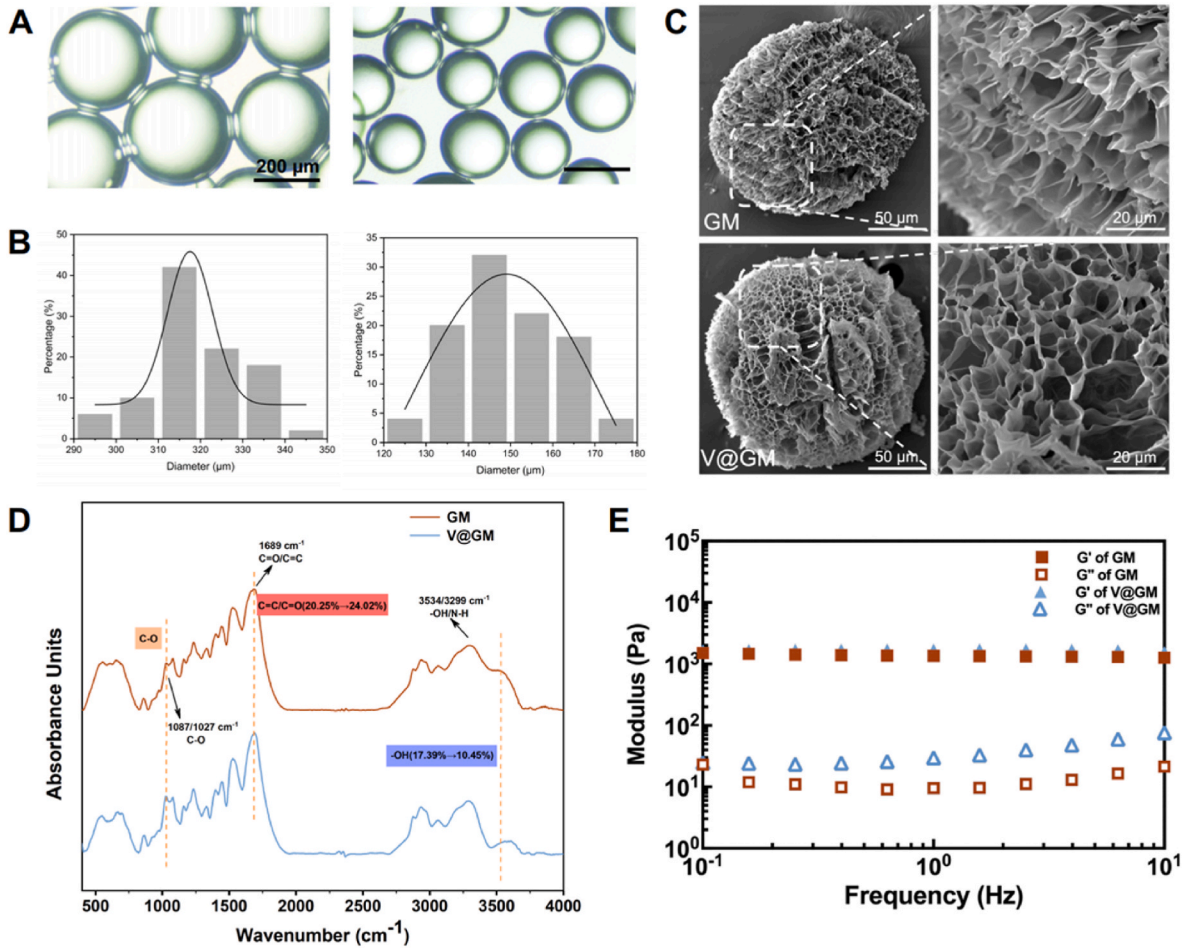

Fig. 1. Characterizations of microspheres. (A, B) Monodisperse GelMA microspheres of two sizes and corresponding particle size distributions (n = 50). (C) SEM images of GelMA microspheres (GM) and vanillin functionalized microspheres (V@GM). (D) FTIR spectra of GM and V@GM. (E) Frequency sweep rheological analysis of GM and V@GM.

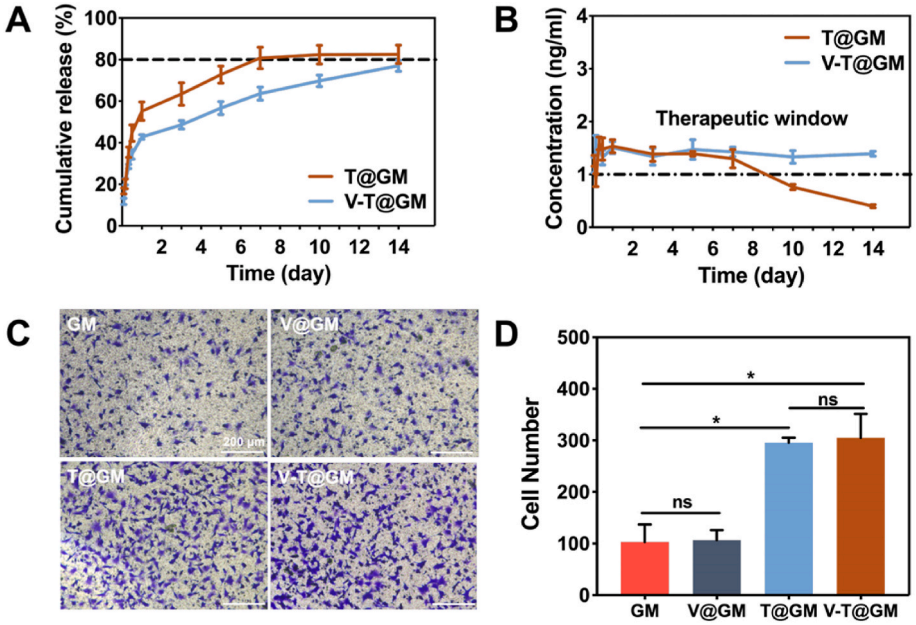

Fig. 2. TGFβ3 controlled release property of functionalized microspheres. (A, B) *In vitro* release kinetics of TGFβ3 in GM and V@GM (n = 3). (C) Representative light photomicrographs of migrated NPCs cultured with microspheres. (D) Quantitative analysis of migrated cell density (n = 3). *, $p < 0.05$; ns, no significant difference.

be observed in both groups during the first day, which may be attributed to the easily spread out of TGFβ3 attached to the surface and the large concentration differences inside and outside of the microspheres. Approximately 55% (55.2 ± 4.4%) of the total was released in the T@GM group compared with only about 40% (42.8 ± 1.1%) in the V-T@GM group. The cumulative release of TGFβ3 in the T@GM group reached about 80% (82.6 ± 4.4%) on the 7th day, while that in the V-T@GM group reached about 80% (77.1 ± 2.7%) on the 14th day (Fig. 2A). The concentration of TGFβ3 was calculated according to the release curve at each time point. The concentration of TGFβ3 was within the therapeutic window for most of the measured period in the V-T@GM group (Fig. 2B). Moreover, the results of the transwell assay suggested that T@GM and V-T@GM both demonstrated the effective recruitment of NPCs at 8 h (Fig. 2C and D), suggesting that the released TGFβ3 retained its biological activity.

3.4. Anti-inflammatory effect of functionalized microspheres in vitro

To mimic the microenvironment to which NPCs are exposed in the setting of IVDD as much as possible, LPS was used to induce a microenvironment with excessive inflammation *in vitro*. Compared with the GM group (without the treatment of LPS), the successful induction of inflammation by LPS could be evidenced by the increased gene expression levels of *Il1b, Il6, Ptgs2*, and *Tnfa* in LPS-induced NPCs (GM' group) ($p < 0.05$). Further, different microspheres showed different cellular responses to inflammation. The expression levels of these inflammation-related genes were inhibited in both the V@GM and V-T@GM groups ($p < 0.05$). In contrast, there was no statistical difference in the expression levels of inflammation-related genes between the GM' and T@GM groups ($p > 0.05$), suggesting that the anti-inflammatory effects of functionalized microspheres may come from the biomass vanillin (Fig. 3A). The results of COX2 immunofluorescence were consistent with the above. Compared with the GM group (2.4 ± 0.7), treatment with LPS significantly increased the COX2 expression of NPCs

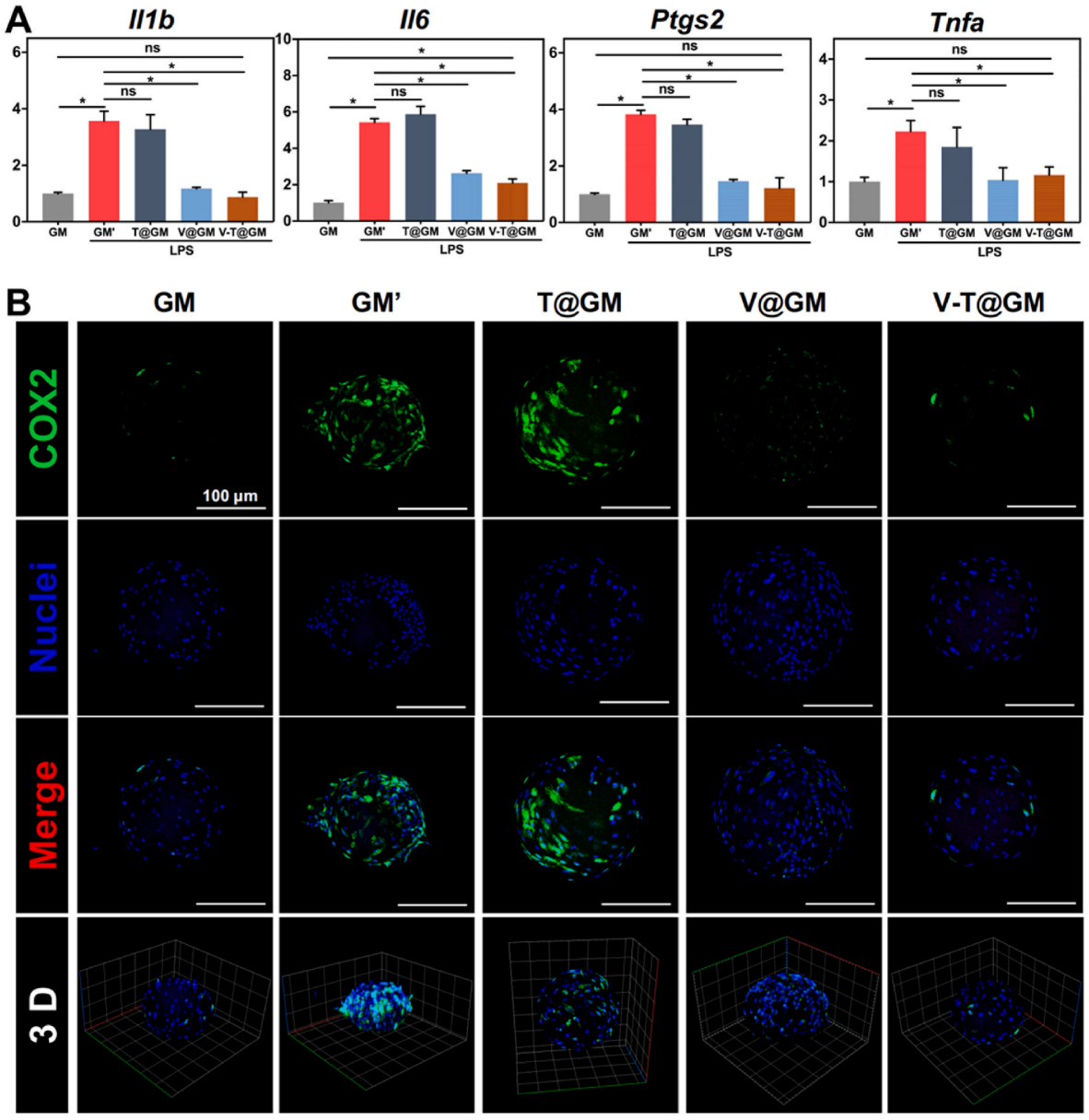

Fig. 3. Anti-inflammatory effect of functionalized microspheres. (A) Quantifications of inflammation-related genes expression (*Il1b*, *Il6*, *Ptgs2*, and *Tnfa*) in NPCs cultured on microspheres by qRT-PCR after 3 days (n = 3). (B) COX2 immunofluorescence images after 5 days. *, $p < 0.05$; ns, no significant difference.

(GM' group, 61.9 ± 14.8) ($p < 0.05$). There is no statistical difference in COX2 expression between the T@GM (50.6 ± 3.0) and GM' groups ($p > 0.05$). Treatment of V@GM (4.1 ± 0.5) or V-T@GM (3.1 ± 0.6) had reduced COX2 expression and showed no statistical difference from the GM group ($p > 0.05$) (Fig. 3B and S7A). These suggest that vanillin grafted onto microspheres still retains good anti-inflammatory properties and can inhibit an overactivation of inflammation in NPCs induced with LPS.

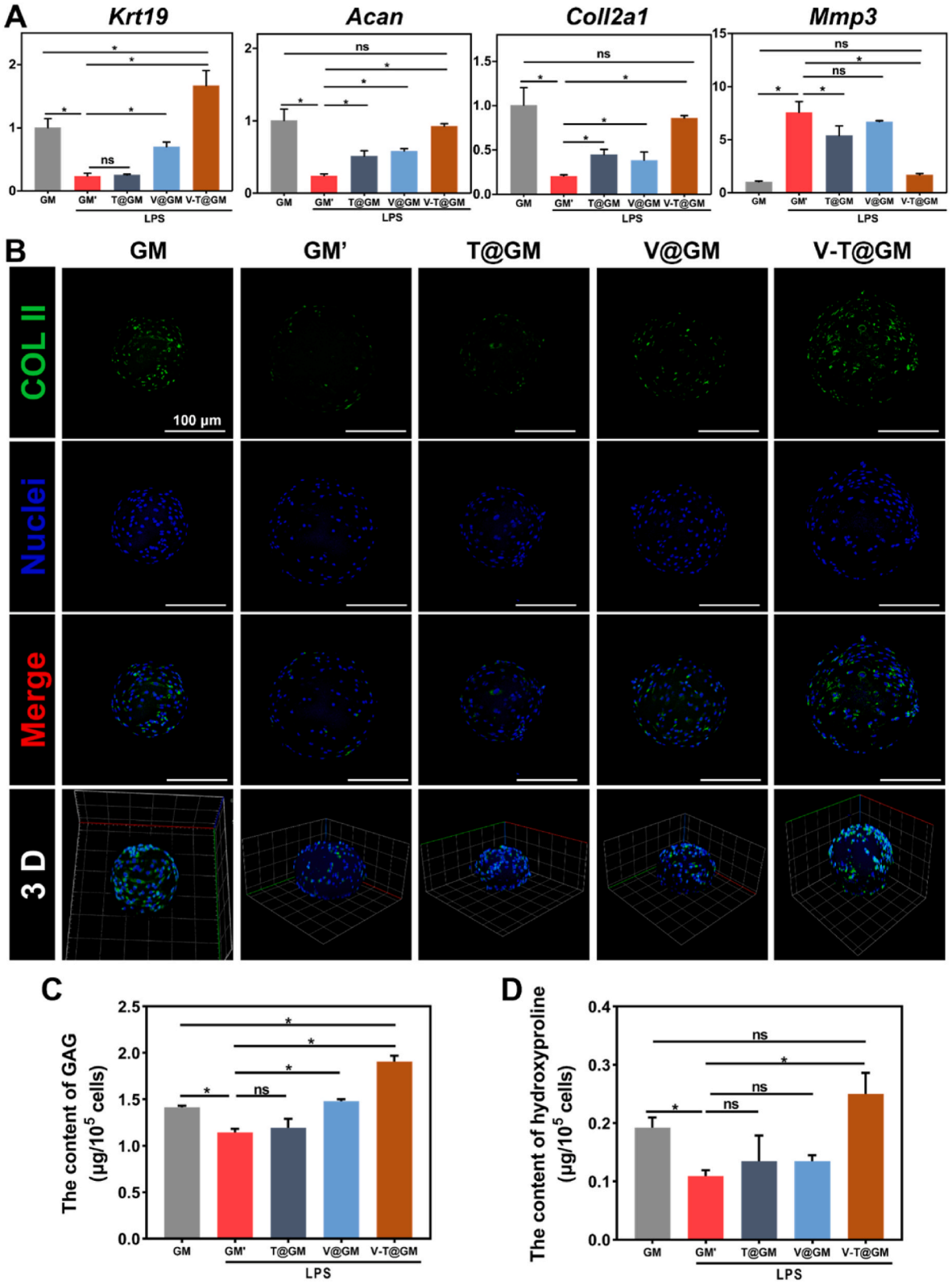

Fig. 4. The matrix metabolism of NPCs on different microspheres with LPS treatment. (A) Quantifications of matrix metabolism-related genes expression (*Krt19, Acan, Col2a1, and Mmp3*) in NPCs on microspheres by qRT-PCR after 3 days (n = 3). (B) COL II immunofluorescence images after 5 days. Quantifications of (C) GAG and (D) hydroxyproline of NPCs after 14 days (n = 3). *, $p < 0.05$; ns, no significant difference.

3.5. Regulation of the anabolism/catabolism by functionalized microspheres in the inflammatory microenvironment

The imbalance of the anabolism/catabolism of ECM in NPCs was closely associated with the local inflammatory microenvironment and initiated and promoted IVDD. We, therefore, investigated the effects of functionalized microspheres on the ECM expression with LPS-treated NPCs. Type II collagen (COL II) and aggrecan are the main components of the ECM in NP tissue and are responsible for the physiological functions of normal IVD. Keratin 19 (KRT19), paired box1 (PAX1), and forkhead box f1 (FOXF1) recognized markers of NPC, have been used to describe the phenotype and status of NPCs [62,63]. qRT-PCR showed that treatment with LPS decreased the expression levels of *Col2a1*, *Acan, Krt19,* and *Pax1* in NPCs cultured on GelMA microspheres (GM' group) compared with the GM group (without treatment with LPS) ($p < 0.05$) (Fig. 4A and S6A). It was also found that the expression levels of these genes in NPCs could be maintained in the V-T@GM group with continuous LPS induction. There was no statistical difference in the expression levels of *Col2a1* and *Acan* between the V-T@GM group and GM group ($p > 0.05$), while *Krt19*, *Pax1,* and *Foxf1* were upregulated ($p < 0.05$) (Fig. 4A and S6B). The expression level of *Mmp3*, a catabolism-related gene in the ECM of NPCs, was significantly downregulated in the V-T@GM group compared with the GM', T@GM, and V@GM groups ($p < 0.05$), there was no statistical difference from the GM group ($p > 0.05$) (Fig. 4A). The results of COL II immunofluorescence were consistent with the above. Compared with the GM group (16.2 ± 3.4), treatment with LPS significantly decreased COL II expression of NPCs (GM' group, 1.2 ± 0.5) ($p < 0.05$). Treatment of T@GM (2.5 ± 0.4) or V@GM (4.3 ± 0.7) showed no statistical difference from the GM' group ($p > 0.05$). COL II expression level was maintained in the V-T@GM group (16.3 ± 2.1) and showed no statistical difference from the GM group ($p > 0.05$) (Fig. 4B and S7B). Although the ECM of chondrocytes is also rich in aggrecan and COL II, the NP matrix can be distinguished from cartilage by different glycosaminoglycans (GAG) and hydroxyproline (HYP) ratios. Because of the physiologic importance of ECM production by NPCs, aggrecan and collagen II should be included in any discussion about NP phenotypic markers [40,63]. Therefore, we also measured the contents of GAG and HYP secreted by the NPCs cultured on different microspheres. Compared with the GM group (GAG: 1.41 ± 0.019, HYP: 0.19 ± 0.017), LPS induction simultaneously reduced the contents of both (GM' group, GAG: 1.15 ± 0.040, HYP: 0.11 ± 0.010) ($p < 0.05$). Treatment of V-T@GM (GAG: 1.91 ± 0.022, HYP: 0.25 ± 0.036) maintained the content of hydroxyproline ($p > 0.05$) and promoted the accumulation of GAG ($p < 0.05$) compared with the GM group, which also confirmed the results of COL II immunofluorescence. Treatment of V@GM (GAG: 1.48 ± 0.022, HYP: 0.13 ± 0.010) maintained GAG content but did not contribute to the secretion of hydroxyproline. The contents of both in the T@GM group (GAG: 1.20 ± 0.095, HYP: 0.13 ± 0.044) showed no statistical deference from the GM' group in a setting of inflammation caused by LPS ($p > 0.05$) (Fig. 4C and D). Notably, the results showed that there was no statistical difference in the ratios of GAG and HYP among groups (Fig. S8). And the ratios presented in each group of this experiment were all significantly higher than those in cartilage tissue, indicating to a certain extent that inflammation caused by LPS reduced the content of ECM in NPCs, including aggrecan and COL II, but it did not seem to make them exhibit characteristics like ECM in cartilage. These results suggest that functionalized microspheres loaded with TGFβ3 can promote ECM synthesis and inhibit the hyperactive degradation in the inflammatory microenvironment. Notably, neither TGFβ3 (T@GM group) nor vanillin (V@GM group) treatment alone achieved similar effects.

3.6. Potential signaling pathway for the therapeutic effects of functionalized microspheres

To understand the underlying molecular mechanisms for how the functionalized system affects the therapy and regeneration, RNA-seq was used to investigate the differentially expressed genes (DEGs) between the NPCs cultured on GM and V-T@GM after LPS treatment for 3 days. Compared with the GM group, 741 genes were upregulated, and 1042 genes were downregulated in NPCs cultured on V-T@GM, as shown in a volcano plot ($|\log_2 FC| \geq 1$ & $p < 0.05$) (Fig. 5A). As shown on the heatmap, compared with the GM group, the expression levels of a series of inflammation-related genes *Il6*, *Nos2*, *Tnfsf13*, and *Ptger2*, as well as ECM catabolism-related genes *Mmp3*, *Mmp13, Adamts5*, and *Adamts9*, were significantly downregulated in the NPCs of the V-T@GM group. ECM synthesis-related genes *Tgfbi*, *Col2a1*, and *Chsy3* were upregulated (Fig. 5B). Gene ontology (GO) analysis showed that these DEGs were mainly associated with the compositions of the collagen fibrils and the ECM, the negative regulation of the inflammatory response, and cell adhesion, migration, and proliferation (Fig. 5C). These biological processes are what we expect the functionalized system to be able to regulate, such as inhibiting the overactive inflammation, promoting the migration, adhesion, and proliferation of NPCs, and regulating the catabolism/anabolism of the ECM. Additionally, compared with the GM group, Gene Set Enrichment Analysis (GSEA) demonstrated that the "cytokine receptor activity", "collagen catabolic process", "acute phase response", and "cellular senescence" were all markedly inhibited in the V-T@GM group (Fig. 5E and S9). To identify the potential signaling pathways involved in these processes, Kyoto Encyclopedia of Genes and Genomes (KEGG) pathway enrichment analysis was performed. The results showed that the phosphatidylinositol 3-kinase (PI3K)-Akt signaling pathway was downregulated in the treatment group (Fig. 5D). In accordance with this, western blotting of AKT and phosphorylated AKT confirmed the results of RNA-seq. AKT and phosphorylated AKT (*p*-AKT) levels were both upregulated in the NPCs treated with LPS and reversed by V@GM and V-T@GM to a certain extent (Fig. 5F). AKT is upstream of NF-κB and mTOR signaling, and its activation results in the amplification of the inflammatory cascade and cartilage matrix loss and remodeling [41,42]. It is therefore believed that functionalized microspheres saved the NPCs at least partially from the overactivated Akt signaling caused by LPS.

3.7. Regenerative performance of functionalized microspheres in vivo

3.7.1. Imaging evaluation

To investigate the effects of different microspheres on the treatment of IVDD, they were injected into the damaged NP tissue of the rat IVDD model. An H_2O_2 probe, Lipo@HRP&ABTS, and photoacoustic (PA) imaging were used to measure the level of H_2O_2 in the damaged NP tissues of different groups on the 7th day. Compared with normal tissue (0.21 ± 0.03), injury markedly increased the local level of H_2O_2 in NP tissue (0.97 ± 0.04) ($p < 0.05$). Inhibition of increasing levels of H_2O_2 was observed in both the T@GM (0.78 ± 0.08) and V@GM groups (0.53 ± 0.01, $p < 0.05$). The signal levels detected in the V-T@GM group (0.35 ± 0.02) were lower than all other groups except for the sham group ($p < 0.05$) (Fig. 6A and C), which indicates that the functionalized system possesses an excellent ability to eliminate H_2O_2 and inhibit oxidative stress *in vivo*.

Imaging is a reliable indicator of the degeneration and repair of IVD. X-ray and magnetic resonance imaging (MRI) were performed at the 4th and 8th week to assess reparative effects. Compared with the sham group (4 weeks: 100.0 ± 5.8%, 8 weeks: 100.0 ± 3.5%), the IVD height in the defect group (4 weeks: 43.6 ± 5.9%, 8 weeks: 36.4 ± 11.0%) significantly decreased after needle puncture ($p < 0.05$). Injections of V@GM (4 weeks: 76.3 ± 7.9%, 8 weeks: 31.5 ± 8.3%) and T@GM (4 weeks: 58.8 ± 9.2%, 8 weeks: 49.6 ± 8.5%) slowed the decrease in IVD height to a certain extent after 4 weeks but was not responsible for maintaining IVD height at the 8th week ($p < 0.05$), showing a time-dependent decline. The best results were achieved with V-T@GM (4 weeks: 86.3 ± 14.1%, 8 weeks: 87.1 ± 9.9%), which maintained IVD height at both time points and showed no statistical difference from the

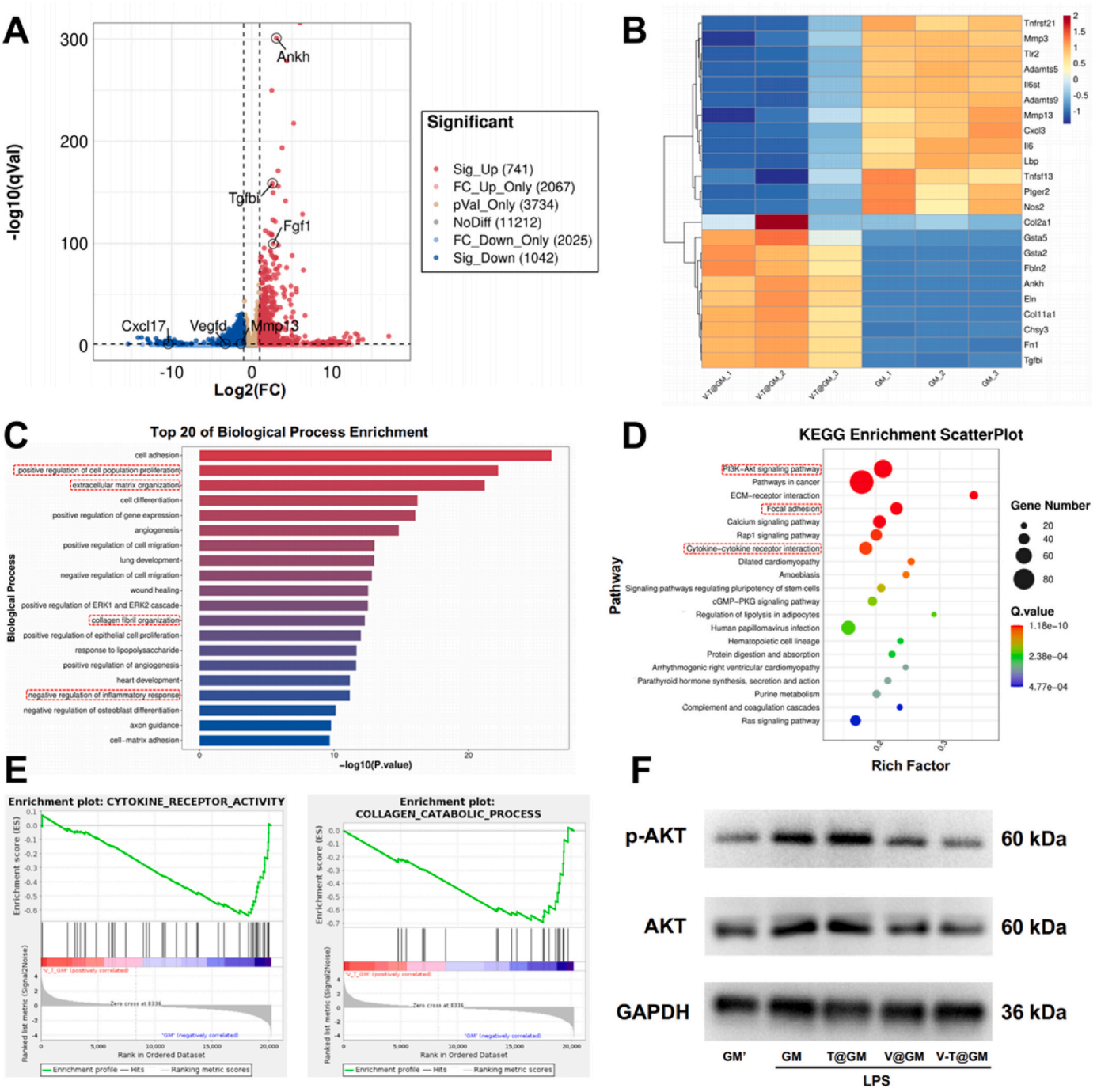

Fig. 5. Transcriptomic analysis. (A) Volcano plot of DEGs. Red dots indicated upregulated genes; Blue dots indicated downregulated genes. (B) Heatmap showed a series of DEGs related to inflammation and matrix metabolism in NPCs. (C) GO analysis showed the top 20 biological processes involved in DEGs. (D) KEGG enrichment bubble plot showed the top 20 pathways involved in DEGs. (E) GSEA showed that the "cytokine receptor activity" and "collagen catabolic process" were inhibited in the V-T@GM group. (F) Western blotting of AKT and *p*-AKT.

sham group ($p > 0.05$) (Fig. 6B and E). T2-weighted signals in MRI corresponds with the water content of NP tissue. Compared with the normal tissue, the NP signal markedly decreased after surgery (4 weeks: 16.0 ± 2.8%, 8 weeks: 10.9 ± 9.3%) ($p < 0.05$). Injections of V@GM (4 weeks: 20.8 ± 8.0%, 8 weeks: 27.0 ± 11.9%) and T@GM (4 weeks: 21.7 ± 1.9%, 8 weeks: 13.5 ± 3.1%) did not help retain NP signal ($p < 0.05$). The V-T@GM group (4 weeks: 73.7 ± 14.4%, 8 weeks: 77.2 ± 11.4%) had the highest relative NP water content at both time points compared with the V@GM and T@GM groups ($p < 0.05$) (Fig. 6B and D).

3.7.2. *Histology evaluation*

Samples were collected at the 4th and 8th weeks after surgery. And the gross morphologies of the IVD was shown in Fig. 7A. It can be seen that the structures of the IVD were significantly damaged in the defect group at two time points after surgery. The T@GM and V@GM groups showed similar time-dependent degeneration, with loss of NP tissue and structural destruction at the 4th and 8th week. The best results were shown in the V-T@GM group, which retained the NP tissue and effectively maintained the normal structure of IVD. Histological sections were collected at the 4th and 8th weeks after surgery. As shown in H&E and SO/FG staining images, the structures of the IVD were significantly

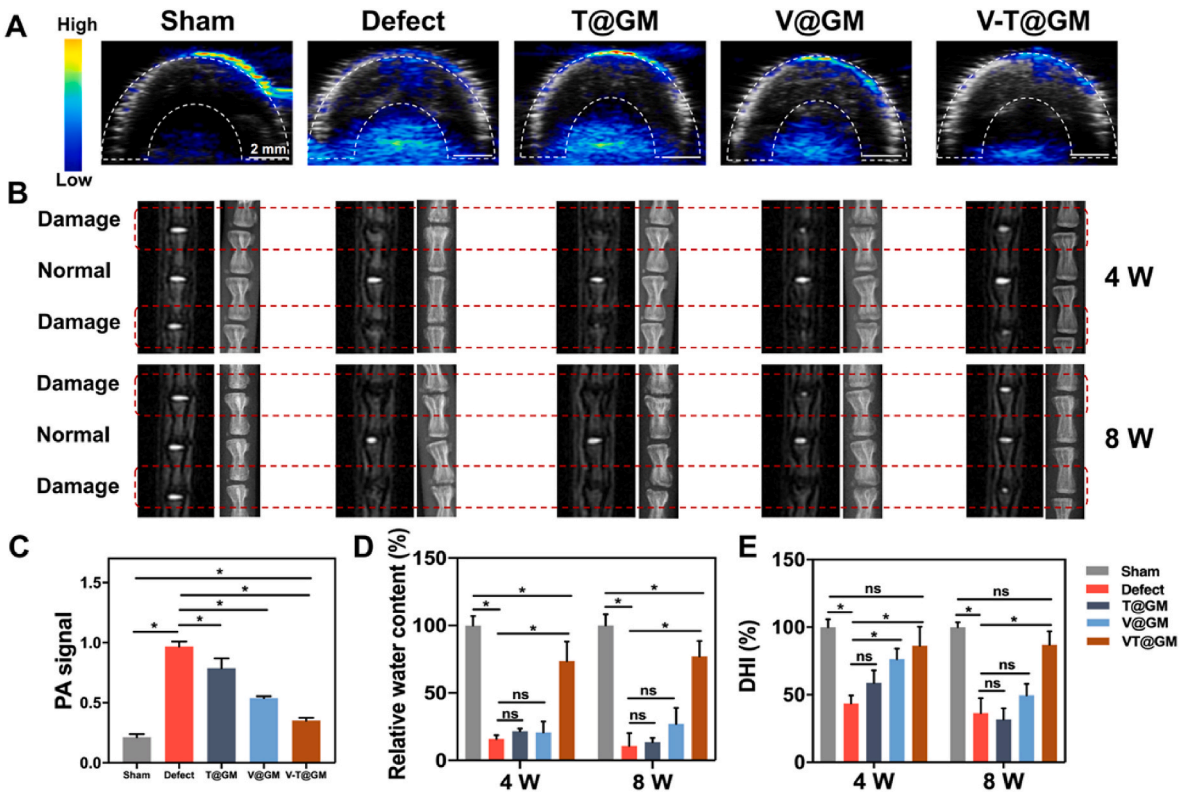

Fig. 6. Imaging evaluation of the animal experiment. (A) PA images of NP tissue *in situ* 7 days after injections of different microspheres. (B) X-ray images (right) and MRI images (left) of the rats' IVDs (marked by red wireframe) after 4 weeks and 8 weeks. Quantitative analyses of (C) PA signals (n = 3), (D) DHI% (n = 3), and (E) the optical density of IVDs (n = 3). *, $p < 0.05$; ns, no significant difference.

damaged after the operation. The annulus fibrous (AF) tissue defect caused by the needle could be observed, and the NP tissue of the defect group almost disappeared at 4 weeks (Fig. 7B). Degeneration continued to worsen over time. The normal structure of the IVD could no longer be identified and had been replaced by disordered tissue without cells and defined borders at 8 weeks, which indicates that the injury involved the cartilage endplate (CE) and AF in the defect group (Fig. 7C). However, tissue degeneration and structural damage to the IVD was inhibited in the V-T@GM group. The CE was intact and most of the NP tissue remained in the IVD at both the 4th and 8th week, with clear and defined borders between the NP and AF (Fig. 7B and C). However, in both the T@GM and V@GM groups, the NP tissue content gradually fell along with the destruction of the normal IVD structure. The degeneration got worse in the T@GM and V@GM groups at the 8th week and was equivalent to the defect group (Fig. 7C and E). Interestingly, the morphology of the NP tissue changed in addition to alterations in its content. Compared with the sham group, it was almost devoid of the large vacuoles in the gelatinous structure of the NP tissue in the V-T@GM group (Fig. 7B and C). Rats still retain the notochordal cells as stem cells in their NP tissue, which is responsible for the presence of large vacuoles in the matrix. And both physiological stimuli like induction of specific growth factor and pathological stimuli like needle puncture injury will induce the transition of notochordal cells into NPCs with the disappearance of vacuoles [40]. Based on previous reports and our results, we hypothesized that the differentiation of notochordal cells to NPCs caused by puncture injury or TGFβ3 may be responsible for the disappearance of these vacuoles. And the roles of the interesting phenomenon in degeneration or repair need further explorations. Histological scoring at 4 and 8 weeks further demonstrated differences in degeneration and repair between all groups (Fig. 7D and E). These results were consistent with our immunohistochemical staining results. The content of COL II in the V-T@GM group was higher than the defect, T@GM, and V@GM groups at 4 and 8 weeks (Fig. 7B and C). The results of aggrecan immunohistochemical staining showed the same changes as COL II. This important component of ECM in NP was almost completely lost in the defect, T@GM, and V@GM groups. The high aggrecan expression could be observed along with intact structure of the IVD in the V-T@GM group (Fig. S12). Immunohistochemical staining of COX2 was used to investigate the anti-inflammatory effect of functionalized microspheres *in vivo*. Compared with the sham group, the expression of COX2 in AF, CE, and NP tissues in the defect group was significantly increased at two time points. T@GM intervention did not contribute to inhibiting COX2 expression, while COX2 expression was significantly inhibited in the V@GM and V-T@GM groups (Fig. S12). These results are consistent with *in vitro* experiments, suggesting that the functionalized microspheres also have favorable anti-inflammatory effects *in vivo* that may be derived from vanillin.

3.7.3. Biomechanical evaluation

The IVD lies between two adjacent vertebral bodies and perform crucial biological functions, including buffering compressive loads in various directions and proving the spine with flexibility [43]. These functions are due to the specific mechanical behaviors that are generated by the structure of the IVD, including buffering compression loads and rapid stress relaxation [44]. To investigate biological function recovery, we conducted compressive tests and stress relaxation tests on the spinal segment containing the surgical disc 8 weeks after surgery. The stress-strain curve of the sham group showed that the normal IVD can resist increased stress through deformation to a certain range. However, stress rapidly increased in the defect group even when a smaller strain was applied. Both the T@GM group and V@GM group showed no significant improvement while the V-T@GM group showed a larger strain and a slower rise that was closest to the sham group (Fig. 8A). The compressive moduli of all the IVDs are shown in Fig. 8B. The compressive moduli of the sham, defect, T@GM, V@GM, and V-T@GM groups were 1.3 ± 0.1, 2.9 ± 0.1, 2.0 ± 0.1, 2.0 ± 0.1 and 1.5 ± 0.1

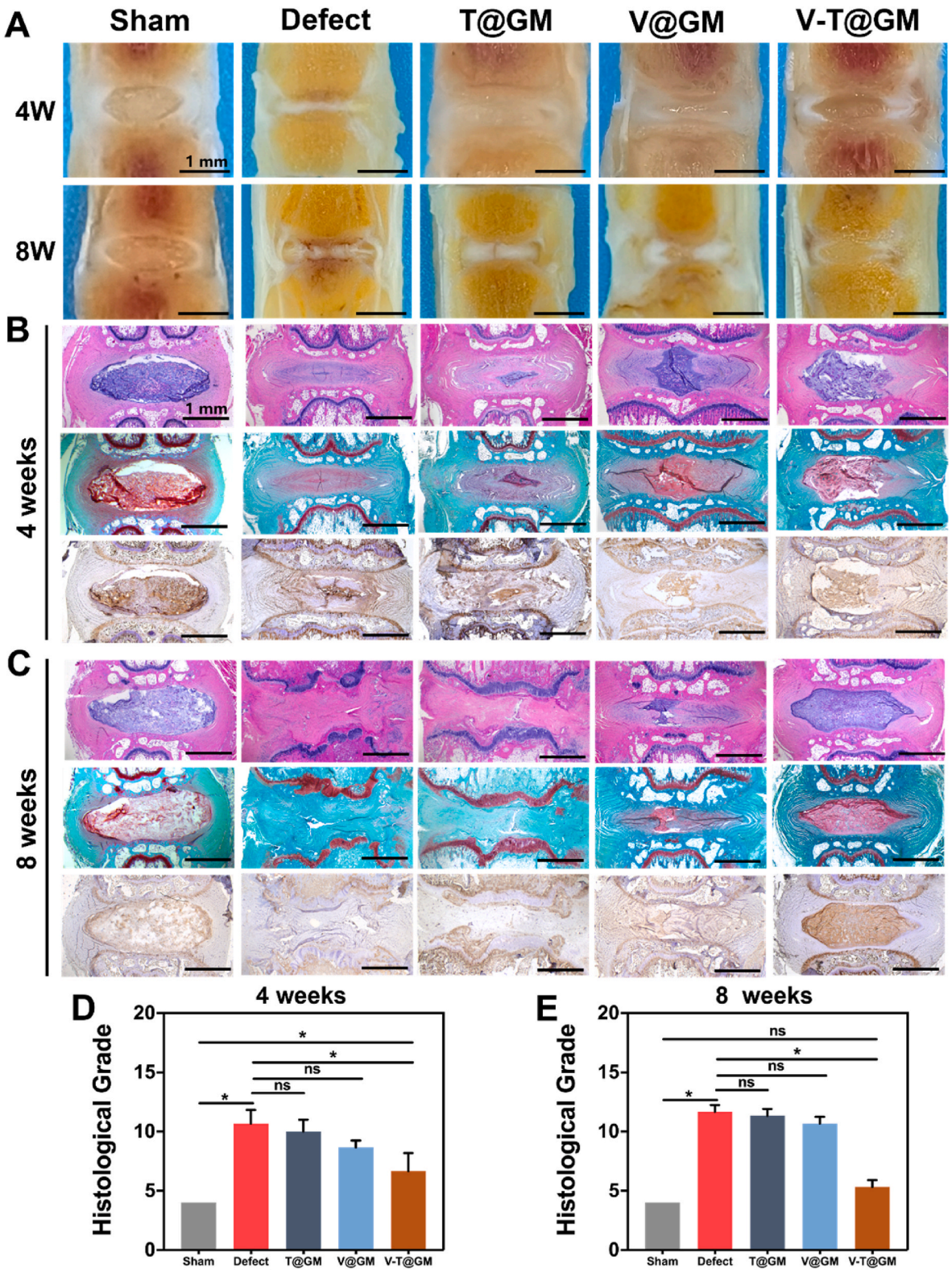

Fig. 7. Histological evaluation of the animal experiment. (A) Gross morphologies of the IVD at 4 weeks and 8 weeks. H&E staining (the first row), SO/FG staining (the second row), and immunohistochemistry staining of COL II (the third row) at (B) 4 weeks and (C) 8 weeks. Histological grade of sections in different groups at (D) 4 weeks and (E) 8 weeks (n = 3). *, $p < 0.05$; ns, no significant difference.

MPa, respectively. The compressive modulus in the defect, T@GM, and V@GM groups increased significantly compared with the sham group ($p < 0.05$), while no significant difference was found between the sham group and V-T@GM group ($p > 0.05$). Rapid stress-relaxation could be observed in normal tissue (Fig. 8C). The rate of stress relaxation under constant strain was quantified as the time for the initially measured stress to relax to half of its original value, or $t_{1/2}$, as defined by a previous study [45]. We found the $t_{1/2}$ in the sham, defect, T@GM, V@GM, and V-T@GM groups were 23.7 ± 1.5, 172.7 ± 14.4, 72.3 ± 9.9, 79.3 ± 10.9 and 40.0 ± 6.0 s, respectively (Fig. 8D). Compared with the sham

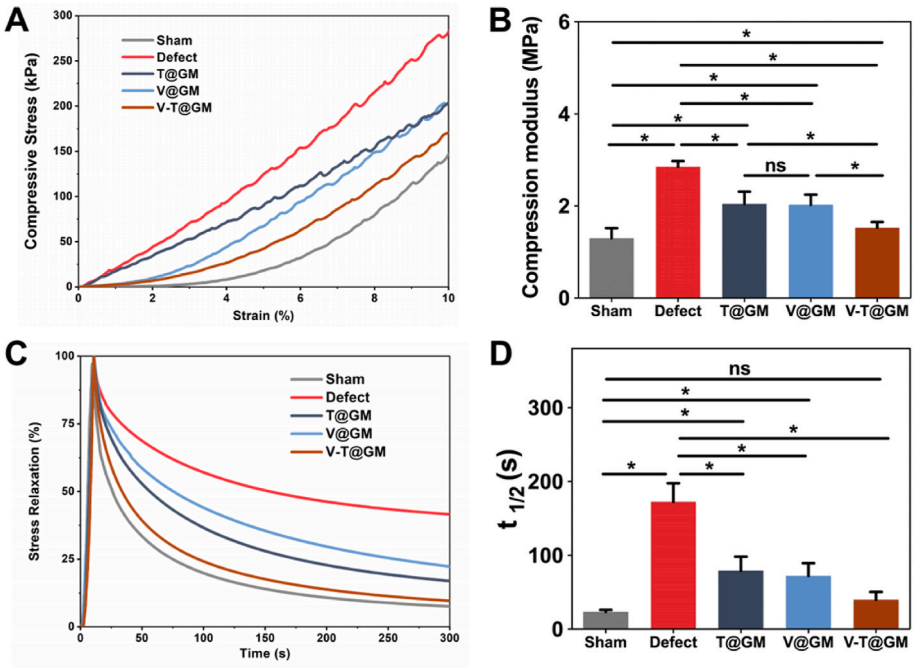

Fig. 8. Biomechanical evaluation of the animal experiment. (A) Stress-strain curves, (B) compression moduli, (C) stress-relaxation curves, and (D) $t_{1/2}$ (n = 3) of IVDs at 8 weeks.

group, the $t_{1/2}$ in the defect, T@GM, and V@GM groups increased significantly ($p < 0.05$), while there was no significant difference between the sham and V-T@GM groups ($p > 0.05$). In general, the V-T@GM implantation helped maintain the biomechanical properties of the IVDs, especially their compressive and stress-relaxation properties.

4. Discussion

In our study, vanillin, a natural small molecule with anti-inflammatory and antioxidant properties, was grafted into GelMA microspheres through the polymerization of monomer VMA and GelMA as part of a novel functionalization strategy for delivery platforms, further preparing uniform and dispersed vanillin functionalized microspheres via microfluidic technology. This functionalization strategy is convenient and universal because of the participation of monomer VMA without changes in the initiation system and functional groups of polymerization behavior. Moreover, we also determined the introduction of VMA at a concentration of 1 mg/mL would not affect the desirable properties of GelMA microspheres, including biocompatibility, cell adhesion, mechanical properties, and porous structure [46]. These desirable properties enable functionalized microspheres to facilitate the loading and release of TGFβ3, maintain their intact structure during delivery, and provide spatial and mechanical supports for the adhesion and proliferation of cells *in vivo* [47].

In addition to targeted local delivery, the important functions of delivery systems are the effective encapsulation and improved release kinetics of therapeutic factors. In some of the current studies, the covalent bonding between growth factors and their carriers is achieved with chemical responses using mainly carboxyl, amine, or cysteine groups, which is beneficial to long-term release [48]. However, growth factors' bioactivity would be affected after chemical coupling. From the perspective of clinical translation, scaffolds pre-loaded with specific growth factors face difficulties with preservation and have limited applications. Unlike previous studies, the improvement of protein release by vanillin is attributed to the numerous dynamic covalent bonds formed between the aldehyde groups and the amino groups. This mild reaction can strictly maintain the biological activities of proteins without damaging their complex and ordered spatial structure, as demonstrated by the effective cell recruitment of functionalized microspheres. These effects were spontaneously achieved through post-drying immersion in the TGFβ3 solution for adsorption-based loading. Loading after the fabrication of the delivery platforms is conducive to changing the type of loaded growth factors to broaden clinical utilization. Functionalized microspheres grafted with vanillin, which serves as a molecular "bridge", can elegantly achieve sustained TGFβ3 release. Based on the extensive development of the modification with methacryloyl anhydride in the field of biomaterials, this vanillin-based functionalization strategy can be used in the designs of various carriers for growth factors delivery.

It has been widely accepted that multiple adverse events play key roles in the progression of IVDD, including an overactive inflammatory microenvironment, oxidative stress, and the imbalance between anabolism and catabolism of the ECM in NPCs [5,6]. On the one hand, these interrelated adverse contributors make it possible to enter the vicious circle of degeneration at any point during IVDD, eventually leading to the same pathology [49]. On the other hand, the harsh microenvironment of the degenerated IVD may be highly hostile to treatment with TGFβ3. Regulation of the abnormal IVDD microenvironment therefore is necessary for any effective IVDD therapy. The results of the NPCs treated with LPS cultured on different microspheres suggested that vanillin modified with methacrylate and grafted into GelMA microspheres still retains its desirable anti-inflammatory and antioxidant properties [50]. Briefly, the anti-inflammatory effects of functionalized microspheres *in vitro* are shown in the downregulation of the expression levels of inflammation-related genes such as *Il1b*, *Il6*, and *Tnfa*, which have been shown to play key roles in the initiation and development of IVDD. They also reduce the expression of COX2 which is a main mediator related to inflammation and discogenic pain. More importantly, the results of the V-T@GM group in the present work showed restoration of the normal microenvironment significantly promotes the bioactivity for TGFβ3 to increase the expression levels of *Krt19*, *Pax1*, *Foxf1*, *Acan*, and *Col2a1* in NPCs, in turn inhibiting that of *Mmp3*. The limited effects of TGFβ3 alone (T@GM) in the setting of extreme inflammation may be due to the crosstalk between signaling pathways and the loss of biological activity [51,52]. Together with more ANAN and Col II secretions by NPCs cultured on V-T@GM, the combined action of vanillin and TGFβ3 in our

functionalized system can suppress overactive inflammation, maintain cellular phenotypes, and promote the secretion and accumulation of ECM under the extreme inflammatory conditions caused by LPS *in vitro*.

H_2O_2, a representative ROS, is closely associated with various pathophysiological processes, such as cancer, cardiovascular, inflammatory, and degenerative diseases, and is another important component of the harsh microenvironment seen in IVDD [53]. While it is commonly accepted that the ROS level increases in the setting of IVDD, there are few reports on ROS detection of the IVD in site. We previously developed a liposomal nanoprobe (Lipo@HRP&ABTS) for PA imaging of H_2O_2 in the tumors, bone defects and osteoporotic bone marrow to reflect inflammation and oxidative stress *in situ* [36,54,55]. We used the Lipo@HRP&ABTS nanoprobe-based PA imaging technique in the present work for *in situ* visualization of H_2O_2 in the NP tissue. The level of H_2O_2 in the damaged NP was markedly higher than in healthy tissue, which suggests that H_2O_2 increase during IVDD. We also identified the role that the functionalized microspheres play in the H_2O_2 scavenging *in vivo*. The antioxidant activity of the functionalized system is derived from the reducing functional groups of vanillin, as has been shown previously [31,56]. Interestingly, the H_2O_2-scavenging effects of V@GM were not as ideal as those of V-T@GM, which may be due to limited tissue repair and homeostasis restoration caused by the absence of TGFβ3.

Healthy NP tissue is a hydrated gel with a water content of more than 80% that consists mainly of NPCs, COL II, and aggrecan. This structure enables it to separate two vertebrae, distribute contact pressures, and provide excellent cushioning performance [43,44]. The degenerated NP is an unorganized fibrous tissue that has largely lost its capacity to bind water under compression, resulting in reduced ability to handle contact pressure and lost intervertebral height [57]. The X-ray and MRI results of our study confirmed that the injection of functionalized microspheres loaded with TGFβ3 (V-T@GM) could maintain intervertebral height and NP water content to the greatest extent compared with other groups. More NP tissue, more structural integrity, and more COL II and ACAN expression could be observed in histological sections at the 4th and 8th weeks in the V-T@GM group. The results of the compression test and stress relaxation time at the 8th week also showed that the function of IVD in the V-T@GM group was closest to the sham group. All of these *in vivo* results confirmed that our cell-free functionalized system could effectively reverse multiple adverse contributors leading to IVDD and facilitate the regeneration of the IVD through the combined action of vanillin and TGFβ3. However, treatment with a single factor, whether it regulates the microenvironment or provides TGFβ3, is not ideal for the long-term management of IVDD.

RNA-seq showed that, compared with the NPCs cultured on GM treated with LPS, the expression levels of genes involved in inflammation and ECM catabolism were inhibited in the V-T@GM group. KEGG pathway enrichment showed that the PI3K-Akt signaling pathway was strongly associated with these effects. PI3K-Akt signaling has been widely studied for its central role in physiology and diseases. Particularly, it is recognized that elevated PI3K-Akt signaling is considered a hallmark of cancer [58,59]. Several studies have reported a strong association between PI3K-Akt signaling and degenerative diseases such as neurodegeneration and osteoarthritis (OA) [60]. In our study, the induction of LPS increased the expression and phosphorylation of AKT in NPCs while functionalized microspheres inhibited this increase to a certain extent. Previous studies have shown that Akt signaling is activated by inflammatory cytokines such as IL-1, IL-6, and TNF-α and promotes the production of MMPs, resulting in cartilage matrix loss and remodeling [41]. Xie et al. noted continuously activated Akt signaling in human OA cartilage as well as in a mouse OA model following surgical destabilization of the medial collateral ligament. Inhibition of Akt signaling can effectively alleviate the OA phenotype [42]. According to previous studies and our results, the elevated Akt signaling in NPCs might be one of the reasons of overactive catabolism of ECM in IVDD and is a potential therapeutic target for IVDD.

However, there are still several limitations in this study that should be noted to improve future work. Firstly, although the content of TGFβ3 released by functionalized microspheres was above the therapeutic threshold currently, the drug load and release kinetics need to be further improved by optimizing the preparation of platforms to broaden the therapeutic window. Secondly, the role of Akt signaling could adopt distinct downstream effectors to perform seemingly opposing functions [61]. There are many differences between a cell culture system *in vitro* and complex changes *in vivo*, together with the limited evidence in our results, limiting the validity of the Akt signaling in associating with IVDD. It is, therefore, necessary to explore the downstream target effects of Akt signaling and its relationship with IVDD in future work. Thirdly, pain assessment and behavioral analysis of rat IVDD models are necessary parts of *in vivo* experiment, which facilitates the comprehensive evaluation of therapeutic effects and the application of functionalized delivery platforms in large animals and clinics. Viscoelasticity is one of the key mechanical characteristics of IVD [44]. Stress-relaxation times cannot comprehensively reflect the changes in the viscoelastic property of IVD. Therefore, these evaluations should be paid more attention to in future work to comprehensively evaluate the degeneration and the effects of therapeutic interventions.

5. Conclusion

This study proposed a functionalization strategy using vanillin to create multifunctional GelMA microspheres that were capable of local delivery of TGFβ3 and treatment of IVDD. The results verified that the functionalized microspheres retained desirable pharmacological values of vanillin and improved release kinetics of TGFβ3. In the setting of extreme inflammation caused by LPS, the combined action of vanillin and TGFβ3 in the functionalized system could relieve overactive inflammation, maintain cellular phenotypes, and promote the accumulation of ECM in NPCs. *In vivo*, the functionalized system permitted the elimination of excess ROS, maintenance of the disc height, water content, intact structure, and biomechanical property, thereby promoting the regeneration of IVD. RNA-seq reconfirmed the therapeutic effects and suggested that these effects may be mediated by targeted inhibition of the Akt signaling. These may form the basis for further exploring the therapeutic mechanism of vanillin and the potential pathogenesis and therapeutic targets of IVDD. In a word, this study provides a novel and simple way for packaging multiple functions into a single delivery platform by using vanillin, which could alleviate the harsh microenvironment and synergize TGFβ3 to promote the regeneration of IVD. This strategy not only holds great promise in IVDD treatment but also provides a good example of the application of natural small molecules in tissue engineering.

CRediT authorship contribution statement

Zhuang Zhu: Conceptualization, Methodology, Validation, Formal analysis, Investigation, Data curation, Writing – original draft, Writing – review & editing, Visualization. **Qifan Yu:** Validation, Formal analysis, Investigation, Writing – review & editing. **Hanwen Li:** Conceptualization, Methodology, Writing – review & editing. **Feng Han:** Validation, Formal analysis, Investigation. **Qianping Guo:** Methodology, Investigation. **Heng Sun:** Visualization, Formal analysis, Investigation. **He Zhao:** Methodology, Formal analysis. **Zhengdong Tu:** Formal analysis, Investigation. **Zhuang Liu:** Methodology, Writing – review & editing. **Caihong Zhu:** Conceptualization, Formal analysis, Funding acquisition, Writing – review & editing. **Bin Li:** Conceptualization, Writing – review & editing, Supervision, Project administration, Funding acquisition.

Declaration of competing interest

The authors declare that they have no known competing financial interests or personal relationships that could have appeared to influence the work reported in this paper.

Acknowledgements

This work was supported by National Natural Science Foundation of China (81925027, 32130059, 81871805 and 82072424), the Priority Academic Program Development (PAPD) of Jiangsu Higher Education Institutions, and the Key Laboratory of Orthopaedics of Suzhou (SZS2022017).

Appendix A. Supplementary data

Supplementary data to this article can be found online at https://doi.org/10.1016/j.bioactmat.2023.05.005.

References

[1] J. Hartvigsen, M.J. Hancock, A. Kongsted, Q. Louw, M.L. Ferreira, S. Genevay, D. Hoy, J. Karppinen, G. Pransky, J. Sieper, R.J. Smeets, M. Underwood, Lancet Low Back Pain Series Working Group, what low back pain is and why we need to pay attention, Lancet 391 (2018) 2356–2367, https://doi.org/10.1016/S0140-6736(18)30480-X.

[2] GBD 2019 diseases and injuries collaborators, global burden of 369 diseases and injuries in 204 countries and territories, 1990-2019: a systematic analysis for the global burden of disease study 2019, Lancet 396 (2020) 1204–1222, https://doi.org/10.1016/S0140-6736(20)30925-9.

[3] A. Cieza, K. Causey, K. Kamenov, S.W. Hanson, S. Chatterji, T. Vos, Global estimates of the need for rehabilitation based on the global burden of disease study 2019: a systematic analysis for the global burden of disease study 2019, Lancet 396 (2021) 2006–2017, https://doi.org/10.1016/S0140-6736(20)32340-0.

[4] D. Hoy, L. March, P. Brooks, F. Blyth, A. Woolf, C. Bain, G. Williams, E. Smith, T. Vos, J. Barendregt, C. Murray, R. Burstein, R. Buchbinder, The global burden of low back pain: estimates from the Global Burden of Disease 2010 study, Ann. Rheum. Dis. 73 (2014) 968–974, https://doi.org/10.1136/annrheumdis-2013-204428.

[5] M. Molinos, C.R. Almeida, J. Caldeira, C. Cunha, R.M. Gonçalves, M.A. Barbosa, Inflammation in intervertebral disc degeneration and regeneration, J. R. Soc. Interface 12 (2015), 20141191, https://doi.org/10.1098/rsif.2014.1191.

[6] V. Francisco, J. Pino, M.Á. González-Gay, F. Lago, J. Karppinen, O. Tervonen, A. Mobasheri, O. Gualillo, A new immunometabolic perspective of intervertebral disc degeneration, Nat. Rev. Rheumatol. 18 (2022) 47–60, https://doi.org/10.1038/s41584-021-00713-z.

[7] R. Medzhitov, Origin and physiological roles of inflammation, Nature 454 (2008) 428–435, https://doi.org/10.1038/nature07201.

[8] M.V. Risbud, I.M. Shapiro, Role of cytokines in intervertebral disc degeneration: pain and disc content, Nat. Rev. Rheumatol. 10 (2014) 44–56, https://doi.org/10.1038/nrrheum.2013.160.

[9] A.N.A. Tosteson, T.D. Tosteson, J.D. Lurie, W. Abdu, H. Herkowitz, G. Andersson, T. Albert, K. Bridwell, W. Zhao, M.R. Grove, M.C. Weinstein, J.N. Weinstein, Comparative effectiveness evidence from the spine patient outcomes research trial: surgical versus nonoperative care for spinal stenosis, degenerative spondylolisthesis, and intervertebral disc herniation, Spine 36 (2011) 2061–2068, https://doi.org/10.1097/BRS.0b013e318235457b.

[10] Z. Buser, A.S. Chung, A. Abedi, J.C. Wang, The future of disc surgery and regeneration, Int. Orthop. 43 (2019) 995–1002, https://doi.org/10.1007/s00264-018-4254-7.

[11] S. Liao, H. Meng, J. Zhao, W. Lin, X. Liu, Z. Tian, L. Lan, H. Yang, Y. Zou, Y. Xu, X. Gao, S. Lu, J. Peng, Injectable adipose-derived stem cells-embedded alginate-gelatin microspheres prepared by electrospray for cartilage tissue regeneration, J. Orthop.Translat. 33 (2022) 174–185, https://doi.org/10.1016/j.jot.2022.03.007.

[12] D. Ghosh Dastidar, S. Saha, M. Chowdhury, Porous microspheres: synthesis, characterisation and applications in pharmaceutical & medical fields, Int. J. Pharm. 548 (2018) 34–48, https://doi.org/10.1016/j.ijpharm.2018.06.015.

[13] P.G. Conaghan, S.B. Cohen, F. Berenbaum, J. Lufkin, J.R. Johnson, N. Bodick, Brief report: a phase IIb trial of a novel extended-release microsphere formulation of triamcinolone acetonide for intraarticular injection in knee osteoarthritis, Arthritis Rheumatol. 70 (2018) 204–211, https://doi.org/10.1002/art.40364.

[14] S. Liao, H. Meng, J. Li, J. Zhao, Y. Xu, A. Wang, W. Xu, J. Peng, S. Lu, Potential and recent advances of microcarriers in repairing cartilage defects, J. Orthop.Translat. 27 (2021) 101–109, https://doi.org/10.1016/j.jot.2020.10.005.

[15] E.R. Seaquist, L. Blonde, J.B. McGill, S.R. Heller, D.M. Kendall, J.B. Bumpass, F. M. Pompilio, M.L. Grant, Hypoglycaemia is reduced with use of inhaled Technosphere® Insulin relative to insulin aspart in type 1 diabetes mellitus, Diabet. Med. 37 (2020) 752–759, https://doi.org/10.1111/dme.14202.

[16] A.R. Tellegen, I. Rudnik-Jansen, M. Beukers, A. Miranda-Bedate, F.C. Bach, W. de Jong, N. Woike, G. Mihov, J.C. Thies, B.P. Meij, L.B. Creemers, M.A. Tryfonidou, Intradiscal delivery of celecoxib-loaded microspheres restores intervertebral disc integrity in a preclinical canine model, J. Contr. Release 286 (2018) 439–450, https://doi.org/10.1016/j.jconrel.2018.08.019.

[17] I. Rudnik-Jansen, A. Tellegen, M. Beukers, F. Öner, N. Woike, G. Mihov, J. Thies, B. Meij, M. Tryfonidou, L. Creemers, Safety of intradiscal delivery of triamcinolone acetonide by a poly(esteramide) microsphere platform in a large animal model of intervertebral disc degeneration, Spine J. 19 (2019) 905–919, https://doi.org/10.1016/j.spinee.2018.10.014.

[18] C. Ai, Y.H.D. Lee, X.H. Tan, S.H.S. Tan, J.H.P. Hui, J.C.-H. Goh, Osteochondral tissue engineering: perspectives for clinical application and preclinical development, J. Orthop.Translat. 30 (2021) 93–102, https://doi.org/10.1016/j.jot.2021.07.008.

[19] V. Volarevic, B.S. Markovic, M. Gazdic, A. Volarevic, N. Jovicic, N. Arsenijevic, L. Armstrong, V. Djonov, M. Lako, M. Stojkovic, Ethical and safety issues of stem cell-based therapy, Int. J. Med. Sci. 15 (2018) 36–45, https://doi.org/10.7150/ijms.21666.

[20] Y. Peng, J. Li, H. Lin, S. Tian, S. Liu, F. Pu, L. Zhao, K. Ma, X. Qing, Z. Shao, Endogenous repair theory enriches construction strategies for orthopaedic biomaterials: a narrative review, Biomater.Translat. 2 (2021) 343–360, https://doi.org/10.12336/biomatertransl.2021.04.008.

[21] A.B. Bello, Y. Kim, S. Park, M.S. Muttigi, J. Kim, H. Park, S. Lee, Matrilin3/TGFβ3 gelatin microparticles promote chondrogenesis, prevent hypertrophy, and induce paracrine release in MSC spheroid for disc regeneration, NPJ Regen. Med. 6 (2021) 50, https://doi.org/10.1038/s41536-021-00160-0.

[22] M.V. Risbud, A. Di Martino, A. Guttapalli, R. Seghatoleslami, V. Denaro, A. R. Vaccaro, T.J. Albert, I.M. Shapiro, Toward an optimum system for intervertebral disc organ culture: TGF-beta 3 enhances nucleus pulposus and anulus fibrosus survival and function through modulation of TGF-beta-R expression and ERK signaling, Spine 31 (2006) 884–890, https://doi.org/10.1097/01.brs.0000209335.57767.b5.

[23] S. Chen, S. Liu, K. Ma, L. Zhao, H. Lin, Z. Shao, TGF-β signaling in intervertebral disc health and disease, Osteoarthritis Cartilage 27 (2019) 1109–1117, https://doi.org/10.1016/j.joca.2019.05.005.

[24] T. Hodgkinson, B. Shen, A. Diwan, J.A. Hoyland, S.M. Richardson, Therapeutic potential of growth differentiation factors in the treatment of degenerative disc diseases, JOR Spine 2 (2019) e1045, https://doi.org/10.1002/jsp2.1045.

[25] R. Tsaryk, A. Gloria, T. Russo, L. Anspach, R. De Santis, S. Ghanaati, R.E. Unger, L. Ambrosio, C.J. Kirkpatrick, Collagen-low molecular weight hyaluronic acid semi-interpenetrating network loaded with gelatin microspheres for cell and growth factor delivery for nucleus pulposus regeneration, Acta Biomater. 20 (2015) 10–21, https://doi.org/10.1016/j.actbio.2015.03.041.

[26] R. Subbiah, R.E. Guldberg, Materials science and design principles of growth factor delivery systems in tissue engineering and regenerative medicine, Adv Healthc Mater 8 (2019), e1801000, https://doi.org/10.1002/adhm.201801000.

[27] J. Clouet, M. Fusellier, A. Camus, C. Le Visage, J. Guicheux, Intervertebral disc regeneration: from cell therapy to the development of novel bioinspired endogenous repair strategies, Adv. Drug Deliv. Rev. 146 (2019) 306–324, https://doi.org/10.1016/j.addr.2018.04.017.

[28] T. Guo, X. Zhang, Y. Hu, M. Lin, R. Zhang, X. Chen, D. Yu, X. Yao, P. Wang, H. Zhou, New hope for treating intervertebral disc degeneration: microsphere-based delivery system, Front. Bioeng. Biotechnol. 10 (2022), 933901, https://doi.org/10.3389/fbioe.2022.933901.

[29] A. Kundu, Vanillin biosynthetic pathways in plants, Planta 245 (2017) 1069–1078, https://doi.org/10.1007/s00425-017-2684-x.

[30] D.P. Bezerra, A.K.N. Soares, D.P. de Sousa, Overview of the role of vanillin on redox status and cancer development, 2016, Oxid. Med. Cell. Longev. (2016), 9734816, https://doi.org/10.1155/2016/9734816.

[31] C. Martinelli, C. Pucci, M. Battaglini, A. Marino, G. Ciofani, Antioxidants and nanotechnology: promises and limits of potentially disruptive approaches in the treatment of central nervous system diseases, Adv Healthc Mater 9 (2020), e1901589, https://doi.org/10.1002/adhm.201901589.

[32] C. Kang, W. Cho, M. Park, J. Kim, S. Park, D. Shin, C. Song, D. Lee, H_2O_2-triggered bubble generating antioxidant polymeric nanoparticles as ischemia/reperfusion targeted nanotheranostics, Biomaterials 85 (2016) 195–203, https://doi.org/10.1016/j.biomaterials.2016.01.070.

[33] Y. Tian, L. Pang, R. Zhang, T. Xu, S. Wang, B. Yu, L. Gao, H. Cong, Y. Shen, Poly-tetrahydropyrimidine antibacterial hydrogel with injectability and self-healing ability for curing the purulent subcutaneous infection, ACS Appl. Mater. Interfaces 12 (2020) 50236–50247, https://doi.org/10.1021/acsami.0c13822.

[34] L. Li, K. Sheng, M. Mannarino, P. Jarzem, H. Cherif, L. Haglund, o-Vanillin modulates cell phenotype and extracellular vesicles of human mesenchymal stem cells and intervertebral disc cells, Cells 11 (2022) 3589, https://doi.org/10.3390/cells11223589.

[35] Y. Peng, X. Qing, H. Shu, S. Tian, W. Yang, S. Chen, H. Lin, X. Lv, L. Zhao, X. Chen, F. Pu, D. Huang, X. Cao, Z. Shao, Proper animal experimental designs for preclinical research of biomaterials for intervertebral disc regeneration, Biomater. Translat. 2 (2021) 91–142, https://doi.org/10.12336/biomatertransl.2021.02.003.

[36] Q. Chen, C. Liang, X. Sun, J. Chen, Z. Yang, H. Zhao, L. Feng, Z. Liu, H_2O_2-responsive liposomal nanoprobe for photoacoustic inflammation imaging and tumor theranostics via in vivo chromogenic assay, Proc. Natl. Acad. Sci. U. S. A. 114 (2017) 5343–5348, https://doi.org/10.1073/pnas.1701976114.

[37] K. Masuda, Y. Aota, C. Muehleman, Y. Imai, M. Okuma, E.J. Thonar, G. B. Andersson, H.S. An, A novel rabbit model of mild, reproducible disc degeneration by an anulus needle puncture: correlation between the degree of disc injury and radiological and histological appearances of disc degeneration, Spine 30 (2005) 5–14, https://doi.org/10.1097/01.brs.0000148152.04401.20.

[38] O. Chaudhuri, L. Gu, M. Darnell, D. Klumpers, S.A. Bencherif, J.C. Weaver, N. Huebsch, D.J. Mooney, Substrate stress relaxation regulates cell spreading, Nat. Commun. 6 (2015) 6365, https://doi.org/10.1038/ncomms7365.

[39] O. Jeon, Y.B. Lee, T.J. Hinton, A.W. Feinberg, E. Alsberg, Cryopreserved cell-laden alginate microgel bioink for 3D bioprinting of living tissues, Mater. Today Chem. 12 (2019) 61–70, https://doi.org/10.1016/j.mtchem.2018.11.009.
[40] M.V. Risbud, Z.R. Schoepflin, F. Mwale, R.A. Kandel, S. Grad, J.C. Iatridis, D. Sakai, J.A. Hoyland, Defining the phenotype of young healthy nucleus pulposus cells: recommendations of the Spine Research Interest Group at the 2014 annual ORS meeting, J. Orthop. Res. 33 (2015) 283–293, https://doi.org/10.1002/jor.22789.
[41] M.A. Greene, R.F. Loeser, Function of the chondrocyte PI-3 kinase-Akt signaling pathway is stimulus dependent, Osteoarthritis Cartilage 23 (2015) 949–956, https://doi.org/10.1016/j.joca.2015.01.014.
[42] J. Xie, J. Lin, M. Wei, Y. Teng, Q. He, G. Yang, X. Yang, Sustained Akt signaling in articular chondrocytes causes osteoarthritis via oxidative stress-induced senescence in mice, Bone Res 7 (2019) 23, https://doi.org/10.1038/s41413-019-0062-y.
[43] H. Jia, X. Lin, D. Wang, J. Wang, Q. Shang, X. He, K. Wu, B. Zhao, P. Peng, H. Wang, D. Wang, P. Li, L. Yang, Z. Luo, L. Yang, Injectable hydrogel with nucleus pulposus-matched viscoelastic property prevents intervertebral disc degeneration, J. Orthop.Translat. 33 (2022) 162–173, https://doi.org/10.1016/j.jot.2022.03.006.
[44] G.T. Desmoulin, V. Pradhan, T.E. Milner, Mechanical aspects of intervertebral disc injury and implications on biomechanics, Spine 45 (2020) E457–E464, https://doi.org/10.1097/BRS.0000000000003291.
[45] J. Lou, R. Stowers, S. Nam, Y. Xia, O. Chaudhuri, Stress relaxing hyaluronic acid-collagen hydrogels promote cell spreading, fiber remodeling, and focal adhesion formation in 3D cell culture, Biomaterials 154 (2018) 213–222, https://doi.org/10.1016/j.biomaterials.2017.11.004.
[46] A.G. Kurian, R.K. Singh, K.D. Patel, J.-H. Lee, H.-W. Kim, Multifunctional GelMA platforms with nanomaterials for advanced tissue therapeutics, Bioact. Mater. 8 (2022) 267–295, https://doi.org/10.1016/j.bioactmat.2021.06.027.
[47] Q. Wei, S. Wang, F. Han, H. Wang, W. Zhang, Q. Yu, C. Liu, L. Ding, J. Wang, L. Yu, C. Zhu, B. Li, Cellular modulation by the mechanical cues from biomaterials for tissue engineering, Biomater.Translat. 2 (2021) 323–342, https://doi.org/10.12336/biomatertransl.2021.04.001.
[48] B. Choi, S. Kim, J. Fan, T. Kowalski, F. Petrigliano, D. Evseenko, M. Lee, Covalently conjugated transforming growth factor-β1 in modular chitosan hydrogels for the effective treatment of articular cartilage defects, Biomater. Sci. 3 (2015) 742–752, https://doi.org/10.1039/c4bm00431k.
[49] P.-P.A. Vergroesen, I. Kingma, K.S. Emanuel, R.J.W. Hoogendoorn, T.J. Welting, B. J. van Royen, J.H. van Dieën, T.H. Smit, Mechanics and biology in intervertebral disc degeneration: a vicious circle, Osteoarthritis Cartilage 23 (2015) 1057–1070, https://doi.org/10.1016/j.joca.2015.03.028.
[50] P. Wang, C. Li, G. Liao, Y. Huang, X. Lv, X. Liu, W. Chen, L. Zhang, Vanillin attenuates proinflammatory factors in a tMCAO mouse model via inhibition of TLR4/NF-kB signaling pathway, Neuroscience 491 (2022) 65–74, https://doi.org/10.1016/j.neuroscience.2022.03.003.
[51] Y. Yang, N. Zhang, F. Lan, K. Van Crombruggen, L. Fang, G. Hu, S. Hong, C. Bachert, Transforming growth factor-beta 1 pathways in inflammatory airway diseases, Allergy 69 (2014) 699–707, https://doi.org/10.1111/all.12403.
[52] B. Bierie, H.L. Moses, Transforming growth factor beta (TGF-beta) and inflammation in cancer, Cytokine Growth Factor Rev. 21 (2010) 49–59, https://doi.org/10.1016/j.cytogfr.2009.11.008.
[53] C.C. Winterbourn, Reconciling the chemistry and biology of reactive oxygen species, Nat. Chem. Biol. 4 (2008) 278–286, https://doi.org/10.1038/nchembio.85.
[54] Q. Chen, J. Li, F. Han, Q. Meng, H. Wang, Q. Wei, Z. Li, F. Li, E. Xie, X. Qin, S. Chen, W. Wang, C. Liu, B. Li, F. Han, A multifunctional composite hydrogel that rescues the ROS microenvironment and guides the immune response for repair of osteoporotic bone defects, Adv. Funct. Mater. 32 (2022), 2201067, https://doi.org/10.1002/adfm.202201067.
[55] J. Li, F. Han, J. Ma, H. Wang, J. Pan, G. Yang, H. Zhao, J. Zhao, J. Liu, Z. Liu, B. Li, Targeting endogenous hydrogen peroxide at bone defects promotes bone repair, Adv. Funct. Mater. 32 (2022), 2111208, https://doi.org/10.1002/adfm.202111208.
[56] C.S.M. Bezerra-Filho, J.N. Barboza, M.T.S. Souza, P. Sabry, N.S.M. Ismail, D.P. de Sousa, Therapeutic potential of vanillin and its main metabolites to regulate the inflammatory response and oxidative stress, Mini Rev. Med. Chem. 19 (2019) 1681–1693, https://doi.org/10.2174/1389557519666190312164355.
[57] J.C. Iatridis, S.B. Nicoll, A.J. Michalek, B.A. Walter, M.S. Gupta, Role of biomechanics in intervertebral disc degeneration and regenerative therapies: what needs repairing in the disc and what are promising biomaterials for its repair? Spine J. 13 (2013) 243–262, https://doi.org/10.1016/j.spinee.2012.12.002.
[58] K. Sun, J. Luo, J. Guo, X. Yao, X. Jing, F. Guo, The PI3K/AKT/mTOR signaling pathway in osteoarthritis: a narrative review, Osteoarthritis Cartilage 28 (2020) 400–409, https://doi.org/10.1016/j.joca.2020.02.027.
[59] D.A. Fruman, H. Chiu, B.D. Hopkins, S. Bagrodia, L.C. Cantley, R.T. Abraham, The PI3K pathway in human disease, Cell 170 (2017) 605–635, https://doi.org/10.1016/j.cell.2017.07.029.
[60] S. Gabbouj, S. Ryhänen, M. Marttinen, R. Wittrahm, M. Takalo, S. Kemppainen, H. Martiskainen, H. Tanila, A. Haapasalo, M. Hiltunen, T. Natunen, Altered insulin signaling in alzheimer's disease brain - special emphasis on PI3K-Akt pathway, Front. Neurosci. 13 (2019) 629, https://doi.org/10.3389/fnins.2019.00629.
[61] M.A. Greene, R.F. Loeser, Function of the chondrocyte PI-3 kinase-Akt signaling pathway is stimulus dependent, Osteoarthritis Cartilage 23 (2015) 949–956, https://doi.org/10.1016/j.joca.2015.01.014.
[62] X. Zhou, N. Shen, Y. Tao, J. Wang, K. Xia, L. Ying, Y. Zhang, X. Huang, J. Hua, C. Liang, Q. Chen, F. Li, Nucleus pulposus cell-derived efficient microcarrier for intervertebral disc tissue engineering, Biofabrication 15 (2023), 025008, https://doi.org/10.1088/1758-5090/acb572.
[63] Y. Zhang, Y. Wang, X. Zhou, J. Wang, M. Shi, J. Wang, F. Li, Q. Chen, Osmolarity controls the differentiation of adipose-derived stem cells into nucleus pulposus cells via histone demethylase KDM4B, Mol. Cell. Biochem. 472 (2020) 157–171, https://doi.org/10.1007/s11010-020-03794-8.